The Company of Biologists

RESEARCH ARTICLE

Cell cycle-dependent palmitoylation of protocadherin 7 by ZDHHC5 promotes successful cytokinesis

Nazlı Ezgi Özkan[1,2], Berfu Nur Yigit[1], Beste Senem Degirmenci[1], Mohammad Haroon Qureshi[1], Gamze Nur Yapici[1], Altuğ Kamacıoglu[1], Nima Bavili[3], Alper Kiraz[3,4] and Nurhan Ozlu[1,2,*]

ABSTRACT

Cell division requires dramatic reorganization of the cell cortex, which is primarily driven by the actomyosin network. We previously reported that protocadherin 7 (PCDH7) gets enriched at the cell surface during mitosis, which is required to build up the full mitotic rounding pressure. Here, we report that PCDH7 interacts with and is palmitoylated by the palmitoyltransferase, ZDHHC5. PCDH7 and ZDHHC5 colocalize at the mitotic cell surface and translocate to the cleavage furrow during cytokinesis. The localization of PCDH7 depends on the palmitoylation activity of ZDHHC5. Silencing PCDH7 increases the percentage of multinucleated cells and the duration of mitosis. Loss of PCDH7 expression correlates with reduced levels of active RhoA and phospho-myosin at the cleavage furrow. This work uncovers a palmitoylation-dependent translocation mechanism for PCDH7, which contributes to the reorganization of the cortical cytoskeleton during cell division.

KEY WORDS: Cytokinesis, Mitosis, Plasma membrane, Protocadherin, PCDH7, Palmitoylation, ZDHHC5, Cleavage furrow, Actomyosin, Plasticity, BioID

INTRODUCTION

Cell division is central to life, driving many vital cellular events such as proliferation, propagation, development and regeneration (Rieder and Khodjakov, 2003). As the cell progresses into mitosis, its morphology and surface undergo dramatic reshaping. Adherent cells transiently round up during mitosis to fulfill the geometric demand of cell division for accurate chromosome segregation (Lancaster et al., 2013; Stewart et al., 2011b). As chromosomes segregate during anaphase, the contractile ring machinery assembles to physically divide cells into two, and the daughter cells spread back to regain their interphase morphology during cytokinesis (Ramkumar and Baum, 2016). Morphological changes during mitosis and cytokinesis are primarily driven by the reorganization of the actomyosin cytoskeleton network and adhesive systems (Cramer and Mitchison, 1997; Eggert et al., 2006; Rosenblatt, 2008).

At the onset of mitosis, ECT2 activates RhoA at the plasma membrane, which activates its downstream effectors, formins and Rho-associated protein kinase (ROCK) (Ramkumar and Baum, 2016). A member of formins, mDia1 localizes to the cell cortex during mitosis and promotes cortical actin nucleation and polymerization (Bovellan et al., 2014). ROCK is a serine/threonine kinase that activates myosin through the phosphorylation of its two main substrates. Phosphorylation of the myosin-binding subunit of myosin phosphatase (MYPT1) by ROCK inactivates myosin phosphatase (Kimura et al., 1996). ROCK can also directly phosphorylate the myosin regulatory light chain at Ser19 (Amano et al., 1996), which results in the activation of myosin ATPase that stimulates actin crosslinking and actomyosin contractility (Narumiya et al., 2009).

As a cell rounds up, myosin II progressively accumulates at the cell cortex and the amount of myosin at the cortex is correlated with the rounding pressure (Ramanathan et al., 2015). RNAi-based depletion of cortical myosin II substantially impairs the rounding pressure of mitotic cells (Toyoda et al., 2017). Thus, myosin II plays a fundamental role in cortical reorganization during mitosis by promoting cortical tension (Taubenberger et al., 2020). During cytokinesis, communication between the midzone and actin cortex through Rho signaling drives the assembly of the actomyosin contractile ring machinery between segregating chromosomes (Eggert et al., 2006; Wadsworth, 2021). During cytokinesis, the actin cytoskeleton and the ezrin/radixin/moesin (ERM) family, a linker between the plasma membrane and the underlying cortical actin cytoskeleton (Tsukita and Yonemura, 1997), have been shown to play roles in the translocation of plasma membrane proteins to the cleavage furrow through their interaction with the cytoplasmic domains of plasma membrane proteins (Yoshigaki, 1997; Yonemura et al., 1993; Uretmen Kagiali et al., 2020).

Protocadherins (PCDHs) are the largest subgroup of cell surface proteins in the cadherin superfamily (Morishita and Yagi, 2007; Nollet et al., 2000). Although identified as adhesion molecules, the adhesive roles of PCDHs are context dependent. PCDHs can form homophilic and heterophilic interactions that regulate cell–cell adhesion and downstream signaling events in embryonic and adult tissues (Bradley et al., 1998; Chen et al., 2007; Kahr et al., 2013; Kim et al., 1998; Kuroda et al., 2002; Tai et al., 2010). In our previous study (Ozlu et al., 2015), we investigated how cell surface proteins change during cell division and compared the cell surface proteome of interphase and mitotic cells. Our proteomic analysis identified PCDH7 as one of the proteins that is enriched at the mitotic cell surface and retraction fibers. Knockdown of PCDH7 using siRNAs caused a decrease in the mitotic rounding pressure albeit not as strong as myosin II (Ozlu et al., 2015).

Here, we aimed to unravel the underlying mechanism of the cell cycle-dependent localization of PCDH7 and its role in cell division. PCDH7 localizes to the cell surface at the onset of mitosis and concentrates at the cleavage furrow during cytokinesis. A palmitoyltransferase, ZDHHC5, was identified as a proximal interactor of PCDH7. ZDHHC5 interacts with PCDH7, and it

[1]Department of Molecular Biology and Genetics, Koç University, 34450 Istanbul, Türkiye. [2]Koç University Research Center for Translational Medicine (KUTTAM), 34450 Istanbul, Türkiye. [3]Department of Physics, Koç University, 34450 Istanbul, Türkiye. [4]Department of Electrical and Electronics Engineering, Koç University, 34450 Istanbul, Türkiye.

*Author for correspondence (nozlu@ku.edu.tr)

N.E.Ö., 0000-0002-2594-2956; N.O., 0000-0002-5157-8780

targets PCDH7 to the mitotic cortex and cleavage furrow. Cell cycle-dependent localization of PCDH7 depends on palmitoylation and requires ZDHHC5 catalytic activity. PCDH7 depletion reduced active RhoA and myosin II levels at the cleavage furrow and increased the multinucleation rate. We propose that spatiotemporal regulation of PCDH7 through palmitoylation by ZDHHC5 promotes successful cytokinesis in mammalian cells.

RESULTS

PCDH7 localizes to the cleavage furrow during cytokinesis

Our previous study revealed that PCDH7 gets enriched at the cell surface as the cell progresses into mitosis (Ozlu et al., 2015). To probe the spatiotemporal regulation of PCDH7, we analyzed its subcellular localization throughout the cell cycle. For this, we used the PCDH7-GFP-BAC cell line, in which GFP-tagged PCDH7 is expressed under its own promoter using bacterial artificial chromosome (BAC) transgenomics in HeLa Kyoto cells (Poser et al., 2008). Immunostaining of the PCDH7-GFP-BAC cells showed that PCDH7 localized to the cell–cell contacts during interphase (Fig. 1A, top), was enriched at the cell surface and retraction fibers at the onset of mitosis (Fig. 1A, middle), and concentrated at the contractile ring and to a narrow zone within the furrow (Normand and King, 2010) (Fig. 1A, bottom). We observed a similar cleavage furrow (0 min) and equatorial accumulation (3–12 min) of PCDH7 in HeLa S3 cells expressing PCDH7::GFP (Fig. 1B; Movie 1). We observed that the localization of PCDH7 at the cleavage furrow was slightly asymmetric (Fig. 1B, 0 min; Fig. S1A). The cell cycle-dependent localization of PCDH7 prompted us to test whether cytokinesis-specific localization is due to cleavage furrow formation but not due to freshly forming cell–cell contact regions of two daughter cells. To this end, we utilized the monopolar cytokinesis approach (Hu et al., 2008; Karayel et al., 2018; Ozlü et al., 2010), in which cells are arrested in monopolar mitosis by using the kinesin-5 inhibitor S-trityl-L-cysteine (STC), followed by induction of monopolar cytokinesis with the CDK inhibitor purvalanol A. The chromosomes stay around one pole, whereas the plasma membrane forms a bud-like extension where the cleavage furrow is greatly expanded without a cell–cell contact region (Fig. S1B). The cleavage furrow proteins, myosin II, anillin, mDia and RhoA localize to the bud-like extension and it biochemically mimics the cleavage furrow of bipolar cytokinetic cells (Hu et al., 2008; Karayel et al., 2018; Ozlü et al., 2010). PCDH7 was enriched at the plasma membrane of monopolar mitotic cells (Fig. 1C, top), and in monopolar cytokinetic cells, it was concentrated at the budding site, which corresponds to the cleavage furrow-like cortex (Fig. 1C, bottom). These results suggest that the cleavage furrow localization of PCDH7 is independent of its cell–cell contact localization.

PCDH7 is more dynamic at the mitotic cell surface than at the cell–cell contact regions

To examine the mitosis-dependent translocation of PCDH7, we performed fluorescence recovery after photobleaching (FRAP) experiments. The mobility of PCDH7::GFP in interphase and mitotic cells was compared using the PCDH7-GFP-BAC cell line. The GFP signal within the region of interest (ROI) at the plasma membrane of both mitotic (Fig. S1C, top) and interphase (Fig. S1C, bottom) cells was photobleached using a focused laser beam. The fluorescence recovery within the ROI was analyzed (Fig. 1D) using a double normalization algorithm (Phair et al., 2004) and fixed-sized ROI areas (Kappel and Eils, 2004). After photobleaching, a significant difference was not observed between the recovery levels

of PCDH7::GFP in cell–cell contacts during interphase (average recovery 46.6%) and at the plasma membrane during mitosis (average recovery 45%), as shown in Fig. 1E (left). However, PCDH7::GFP recovered significantly faster at the mitotic cell surface with an average FRAP half time of around 62 s, compared to its recovery at the cell–cell contacts in interphase, where the average FRAP half time was around 109 s (Fig. 1E, right). We conclude that PCDH7 is much more dynamic and shows a high turnover rate at the mitotic cell surface in comparison to the cell–cell contact regions.

Depletion of PCDH7 increases the rate of multinucleated cells

Next, we asked about the function of PCDH7 in cell division. Our previous investigation by siRNA-based depletion of PCDH7 revealed that PCDH7 is required for the development of mitotic rounding pressure at the onset of mitosis (Ozlu et al., 2015). To obtain more rigorous data, we used CRISPR-Cas9 genome editing (Ran et al., 2013) to knockout PCDH7 in HeLa S3 cells. PCDH7 was targeted using three individual single guide RNAs (sgRNAs). Control cells were treated with a non-targeting (NT) guide RNA (sgNT) in parallel. The knockout (KO) of PCDH7 in isolated colonies was validated by western blotting analysis (Fig. S1D). One colony (PCDH7sg1) was selected to proceed with phenotypic characterization and sgNT-treated cells were used as a control. PCDH7 expression levels in PCDH7 KO, rescue (PCDH7 KO+PCDH7::GFP) and control (PCDH7 KO+eGFP) cells were also validated by western blotting analysis (Fig. S1E).

Then, we examined the extent of cell division failure in PCDH7 KO cells. When we analyzed the multinucleation percentage in fixed cells, we observed a moderate but statistically significant increase in the multinucleation rate in PCDH7 KO cells (Fig. 2A, middle; Fig. 2B). The expression of PCDH7::GFP in PCDH7 KO (Fig. 2A, right) decreased the multinucleation rate statistically close to the levels seen in the control and rescued the phenotype (Fig. 2B, blue).

The weak but statistically significant multinucleation rate could be due to possible adaptations in PCDH7 KO HeLa S3 cells, which can also adapt to proliferate in suspension (Thilly, 1976). Therefore, we employed siRNA- and endonuclease-prepared siRNA (esiRNA)-based depletion of PCDH7 in adherent HeLa Kyoto and HEK293T cells. HeLa Kyoto cells were treated either with control siRNA or PCDH7 siRNA mix, and PCDH7 depletion at the protein level was confirmed by western blotting (Fig. S2A).

The multinucleation rate increased about twofold in PCDH7 siRNA-treated cells (7.7%) in comparison to control siRNA-treated cells (4.3%) (Fig. 2C). Similarly, in HEK293T cells, which have relatively high PCDH7 expression (Human Protein Atlas, accessed 2022, https://www.proteinatlas.org/ENSG00000169851-PCDH7/cell+line; Karlsson et al., 2021), PCDH7 knockdown (Fig. S2B) significantly increased the multinucleation rate, proportional to the extent of protein depletion (Fig. S2C). HeLa Kyoto cells were treated either with control siRNA or PCDH7 siRNA mix, and PCDH7 depletion at the protein level was confirmed by western blotting (Fig. S2A).

To examine the multinucleation phenotype of PCDH7, we performed live-cell analysis using LifeAct::RFP-expressing cells. In contrast to control cells (Fig. 2D, top; Movie 2), in PCDH7 KO cells, the cleavage furrow ingression started; however, cells were not able to complete cytokinesis and merged back to form multinucleated cells (Fig. 2D, bottom; Movie 3). We noticed that the onset of cleavage furrow formation (27 min in control versus 36 min in PCDH7 KO) and completion of furrow ingression
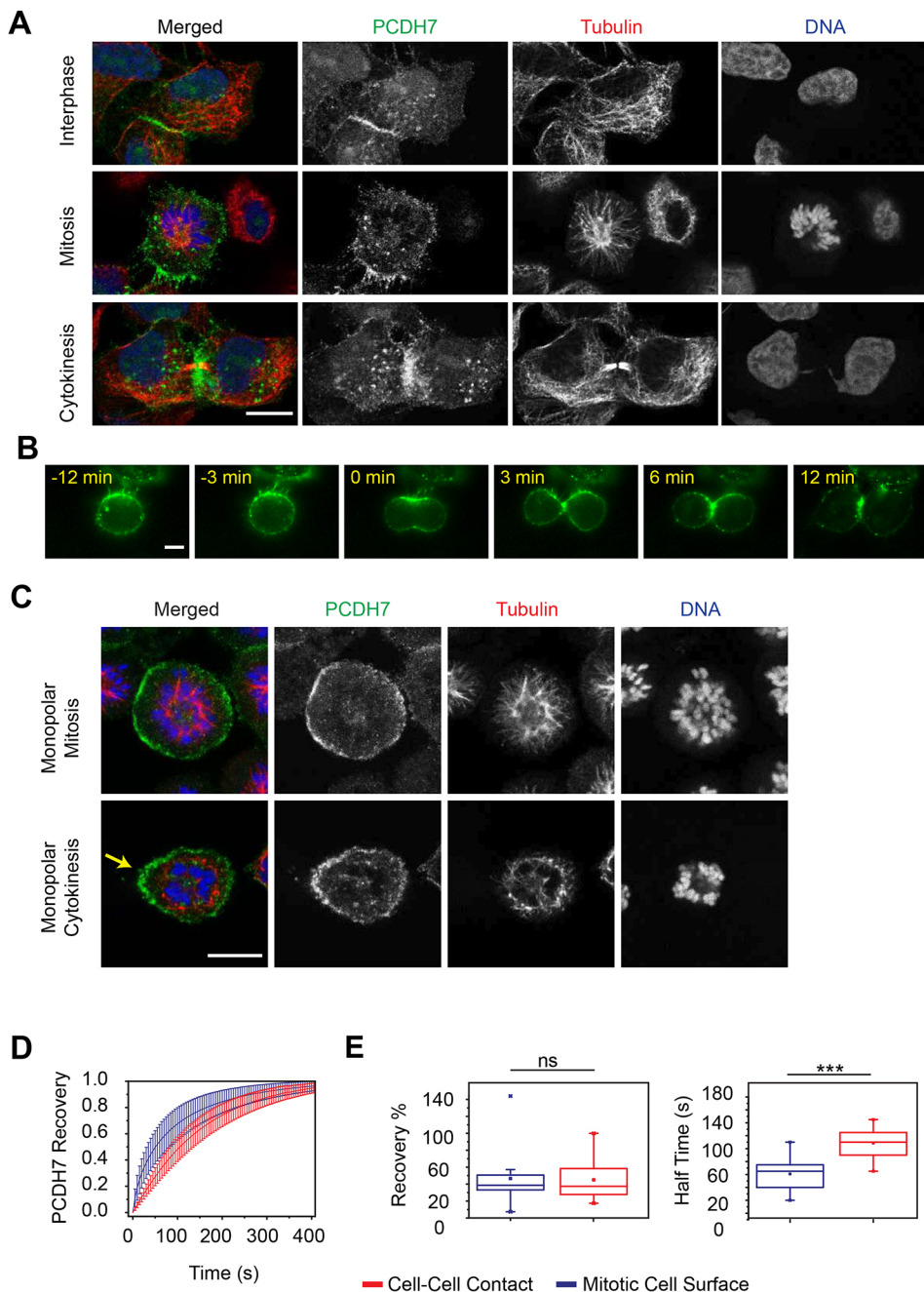
Fig. 1. PCDH7 localizes to the mitotic cell surface and cleavage furrow during cell division. (A) Subcellular localization of PCDH7 (green, anti-GFP), microtubules (red, anti-tubulin) and DNA (blue, DAPI) in PCDH7-GFP-BAC cells in interphase, mitosis and cytokinesis. (B) Live-imaging snapshots of PCDH7::GFP-expressing HeLa cells during cell division. Relative timing according to cleavage furrow ingression is shown in minutes. (C) Subcellular localization of PCDH7 (green, anti-GFP), microtubules (red, anti-tubulin), and DNA (blue, DAPI) in PCDH7-GFP-BAC cells arrested in monopolar mitosis (top) and monopolar cytokinesis (bottom). The yellow arrow indicates the furrow-like cortex. (D) Recovery curve of PCDH7 in the mitotic plasma membrane (blue) (n=23 cells) and cell–cell contact regions (red) (n=25 cells) after photobleaching. (E) Comparison of recovery levels (left) and recovery halftimes (right) in mitotic cell surface (blue) (n=23 cells) and cell–cell contact regions (red) (n=25 cells). Data are representative of eight independent experiments. Statistical analyses used Mann–Whitney U-test. Boxes show the 25–75th percentiles, whiskers represent the minimum and maximum values, and the median is marked with a line. ns, non-significant; ***P<0.001. Scale bars: 10 μm.

(33 min in control versus 42 min in PCDH7 KO) were prolonged in PCDH7 KO cells (Fig. 2D). Quantifying these in siRNA-treated HeLa Kyoto cells revealed a significant delay in both mitosis and cleavage furrow ingression durations (Fig. 2E–G).

The actomyosin network and adhesion molecules are among the proximal interaction partners of PCDH7

To address whether the interaction partners of PCDH7 are involved in its cell cycle-dependent translocation, we employed a proteomic approach using the proximity-dependent biotinylation (BioID) method (Roux et al., 2012). In this method, the protein of interest is fused to a promiscuous biotin ligase BirA*, which biotinylates proteins in proximity to the bait, and the biotinylated proteins are then identified using mass spectrometry. Initial immunofluorescence analysis revealed that the PCDH7::BirA*

recombinant protein exhibited the expected localization pattern in both mitotic and interphase cells, and specifically biotinylated the vicinity (Fig. S3A). To biochemically assess the biotinylation efficiency and specificity, we performed streptavidin affinity purification. Western blotting analysis revealed that PCDH7:: BirA* exhibited efficient and distinct biotinylation patterns (Fig. S3B), and streptavidin affinity purification successfully pulled down PCDH7 (Fig. S3C).

To discover the interphase and mitosis-specific interaction partners of PCDH7, the biotinylated proteins that were isolated from PCDH7::BirA*-expressing mitotic and interphase cells using streptavidin beads were analyzed using liquid chromatography and tandem mass spectrometry (LC-MS/MS). Non-transfected but biotin-supplemented cells were used as a control. The significant interactors were then identified by calculating the spectral
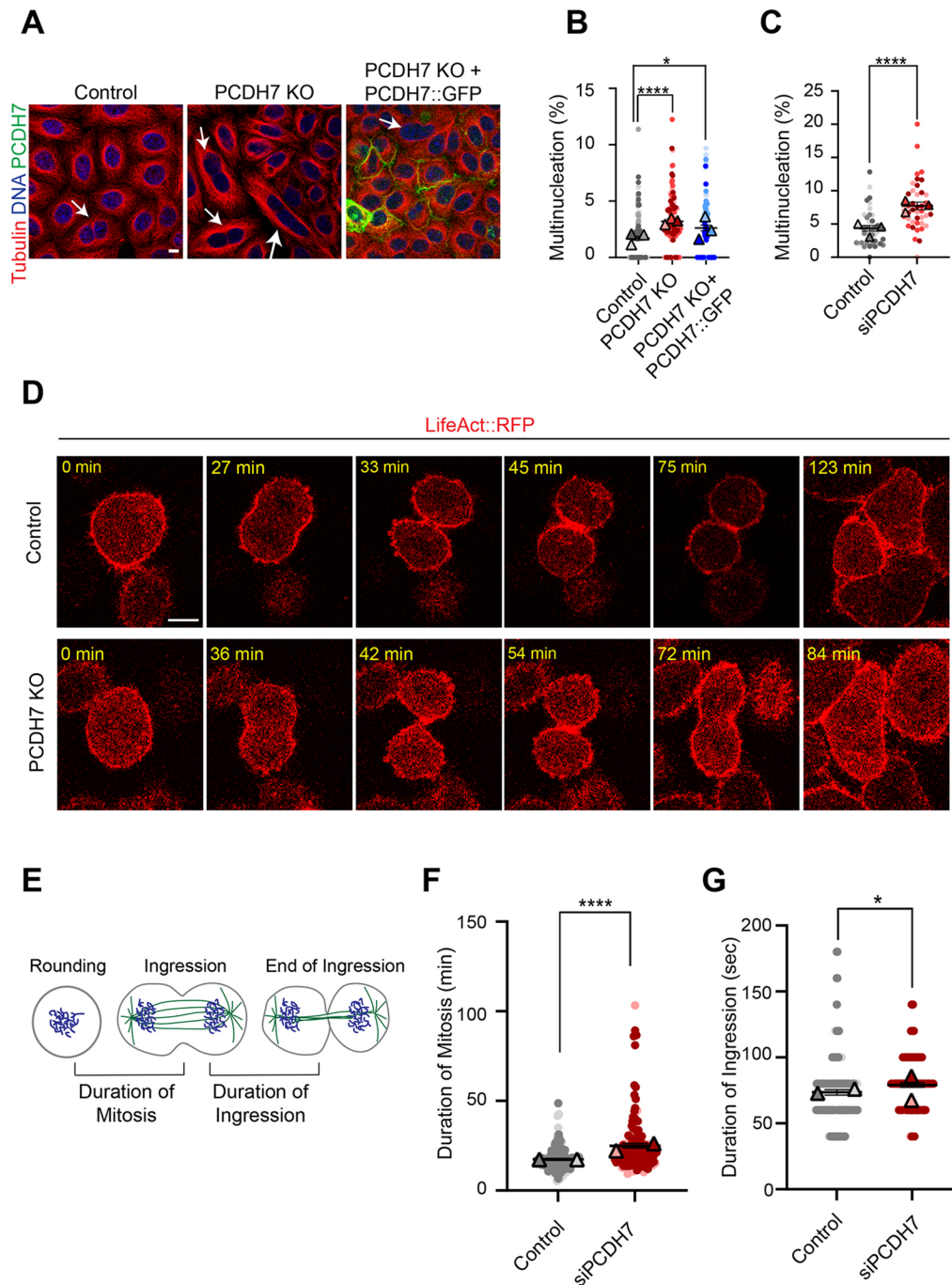
Fig. 2. Depletion of PCDH7 increases the duration of mitosis and the rate of multinucleation. (A) Example images showing multinucleated cells in control (left), PCDH7 KO (middle) and rescue (PCDH7 KO+PCDH7::GFP) conditions (right). Arrows denote multinucleated cells. (B) Quantification of multinucleation percentages of control (gray; mean 1.7%, n=4337 cells), PCDH7 KO (red; mean 3.2%, n=4582 cells) and rescued (PCDH7 KO+PCDH7:: GFP) (blue; mean 2.6%, n=4591 cells) HeLa S3 cells. Forty fields were scored for each group. (C) Quantification of multinucleation in control siRNA (gray; mean 4.3%, n=1988 cells) and PCDH7 siRNA (siPCDH7) (red; mean 7.7%, n=2156 cells)-treated HeLa Kyoto cells. Fourteen fields were scored for each group. For B,C, data are represented as individual percentages for each field (colored circles) and average percentages of three independent biological replicates (colored triangles). Mean with s.e.m. for each group is represented with black lines. Statistical analyses used logistic regression analysis followed by P-value adjustment with the Bonferroni method. (D) Live-imaging snapshots of control (top) and PCDH7 KO cells (bottom) that stably express LifeAct:: RFP. Relative timing according to mitotic rounding is shown in minutes. (E) Schematic representation of the timing in live-cell analysis. 'Duration of mitosis' indicates the time interval between the onset of cell rounding and the onset of furrow ingression. 'Duration of ingression' is measured from the onset of furrow ingression until furrow ingression is completed. (F) Quantification of the mitosis duration in control (gray; 17.42 min mean) and PCDH7 knockdown (siPCDH7) (red; mean 25.00 min) HeLa Kyoto cells. Data are representative of two independent biological replicates (BR) (colored circles) [control, n=64 cells (BR1), n=88 cells (BR2); siPCDH7, n=46 cells (BR1), n=95 cells (BR2)] and average values (colored triangles) are shown. (G) Quantification of the ingression duration in control (gray; mean 73.55 s, gray) and PCDH7 knockdown (siPCDH7) (red; mean 79.15 s) HeLa Kyoto cells. Data are representative of two independent biological replicates (colored circles) [control, n=65 cells (BR1), n=90 cells (BR2); siPCDH7, n=46 cells (BR1), n=85 cells (BR2)] and average values (colored triangles) are shown. For, F,G, mean with s.e.m. for each group is represented with black lines and statistical analyses used two-tailed unpaired t-test. *P<0.05; ****P<0.0001. Scale bars: 10 μm.
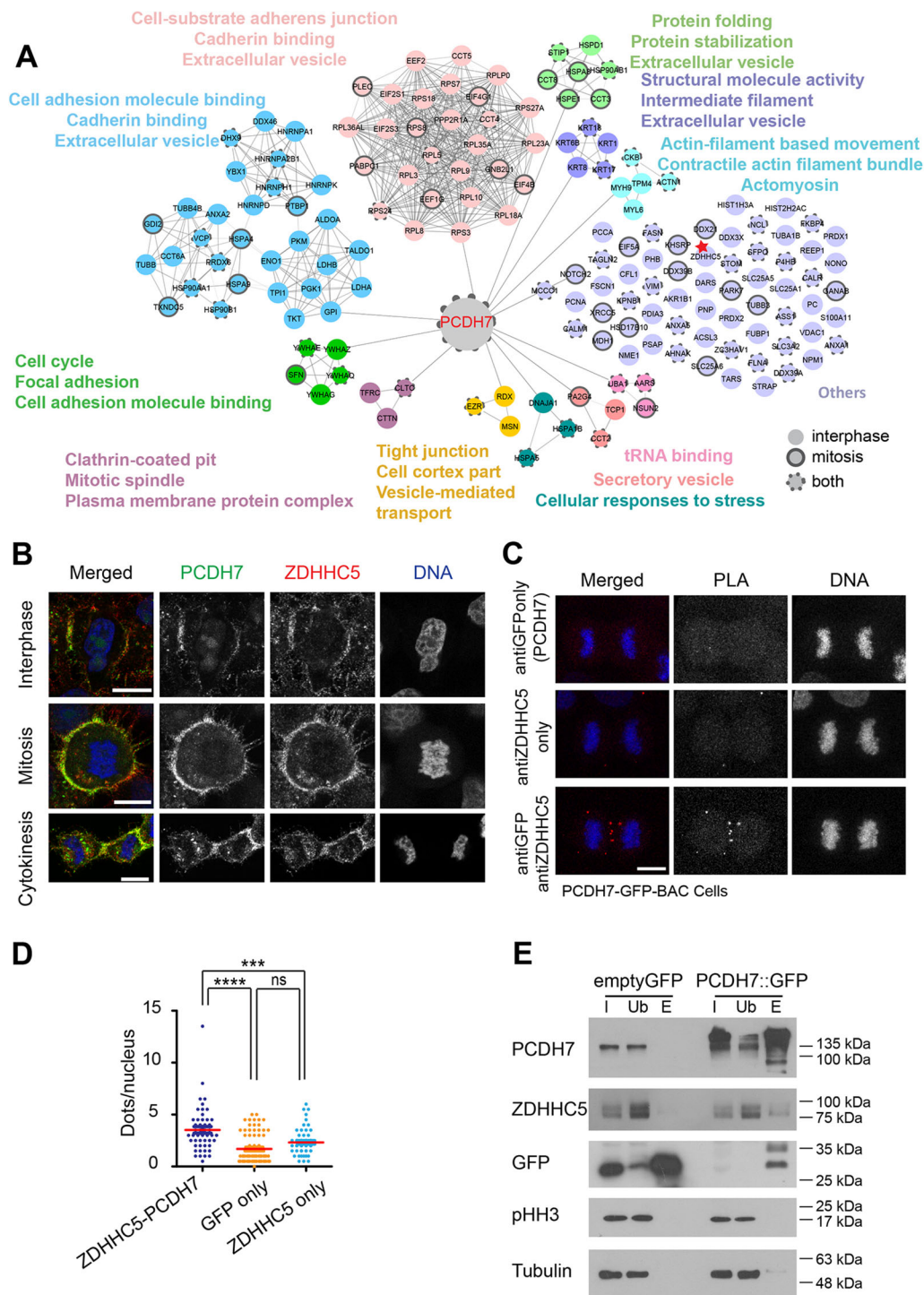
Fig. 3. The proximity interactome of PCDH7 reveals interaction between PCDH7 and ZDHHC5 in a cell cycle-dependent manner. (A) Mapping the proximity interaction networking of PCDH7. Different colors represent the significantly enriched clusters after GO and KEGG enrichment analysis. Interphase-specific interactions are represented with nodes without outlines, mitosis-specific interactors are represented with nodes with solid outlines and common interactors are represented with nodes with dashed outlines. The red star highlights ZDHHC5. (B) Subcellular localization of PCDH7 (green, anti-GFP), ZDHHC5 (red, anti-ZDHHC5) and DNA (DAPI, blue) in PCDH7-GFP-BAC cells during interphase (top), mitosis (middle) and cytokinesis (bottom). (C) Spatial analysis of the interactions between PCDH7 and ZDHHC5 during cytokinesis by in situ proximity ligation assay (PLA). PCDH7-GFP-BAC cells were used for analysis and PCDH7 was targeted using anti-GFP antibodies. Control cells were treated with anti-GFP and anti-ZDHHC5 antibodies separately. The representative images show the interactions between the examined antibody pairs as red fluorescent PLA puncta. DNA is shown in blue (DAPI). (D) Quantification of the PLA puncta observed in cells treated with anti-GFP (PCDH7) antibody only (n=77), anti-ZDHHC5 antibody only (n=59), and anti-GFP and anti-ZDHHC5 antibodies together (n=49). Each image is the maximum-intensity projection of a z-stack. Statistical analysis used one-way ANOVA with Sidak's multiple comparisons test. (E) Pull-down analysis of PCDH7 using GFP-trap approach. HeLa S3 cells that stably express PCDH7::GFP or GFP alone (empty GFP or control) were arrested in mitosis. Whole-cell lysates (input, I), unbound fractions (Ub) and elutes (E) were analyzed by western blotting using antibodies against PCDH7, GFP and ZDHHC5. Phospho-histone H3 (pHH3) was used as a mitosis marker, and α-tubulin was used as the loading control. Image shown in E is representative of at least two repeats. ns, non-significant; ***P<0.001; ****P<0.0001. Scale bars: 10 μm.

count-based fold change between control and PCDH7::BirA*-expressing cells from four biological replicates with a false discovery rate (FDR) of 0.05 (Choi et al., 2015). We identified 78 proteins for mitosis (Table S1) and 129 for interphase cells (Table S2), 47 of which were common in both groups (Table S3). Those proteins were then analyzed using the STRING database (Szklarczyk et al., 2019) and clustered according to Gene Ontology (GO) and KEGG pathway enrichments (Raudvere et al., 2019) using StringApp (Cline et al., 2007; Doncheva et al., 2019). Significant clusters included actomyosin network-related proteins, cell adhesion proteins, cadherin-binding proteins, vesicular proteins and ERM family proteins (Fig. 3A).

PCDH7 interacts with the palmitoyltransferase ZDHHC5 during cell division

Among many interesting candidates, one striking interaction partner of PCDH7 was a palmitoyltransferase (ZDHHC5), which adds the palmityl group to its target proteins. Palmitoylation is a reversible post-translational modification that is known to affect the hydrophobicity, membrane domain interactions and conformation of transmembrane proteins (Blaskovic et al., 2013). To address whether PCDH7 cooperates with ZDHHC5 during cell division, we first visualized the subcellular localization of PCDH7 and ZDHH5 in PCDH7-GFP-BAC cells by using anti-GFP and anti-ZDHH5 antibodies, respectively. During interphase, both PCDH7 and ZDHHC5 localized to the cell–cell contact regions (Fig. 3B, top). During mitosis, both proteins decorated the cell surface and retraction fibers (Fig. 3B, middle) and, as cells proceeded to cytokinesis, they both accumulated at the cleavage furrow (Fig. 3B, bottom). To further verify their colocalization, we applied the proximity ligation assay (PLA) (Söderberg et al., 2006). For this, we used fixed PCDH7-GFP-BAC cells and anti-GFP and anti-ZDHHC5 antibodies to visualize target protein interaction during cytokinesis (Fig. 3C). As expected, we observed a significantly higher signal in cells treated with both primary antibodies than in the control cells that were treated with only one primary antibody (Fig. 3D). The PLA signals were accumulated around the equatorial zone between segregating chromosomes during cytokinesis, which is in line with the immunofluorescence assay (Fig. 3C, bottom).

Given their colocalization, we tested whether PCDH7 physically interacts with ZDHHC5 during mitosis by performing co-immunoprecipitation using the GFP-trap approach in mitotic PCDH7::GFP-expressing cells. We observed that PCDH7 interacts with ZDHHC5 in mitotic cells (Fig. 3E).

Palmitoylation of PCDH7 is required for its localization to the mitotic cell surface and cleavage furrow

The interaction between PCDH7 and ZDHHC5 prompted us to test whether PCDH7 is palmitoylated. To this end, we performed a palmitoylation assay by using acyl-biotin exchange (ABE) chemistry (Wan et al., 2007). PCDH7::GFP-expressing HeLa S3 cells were used to enrich the PCDH7 protein in the samples. Briefly, after performing a high-speed-centrifugation-based membrane enrichment, unmodified cysteine thiol groups were blocked using N-ethylmaleimide (NEM). Half of the sample was treated with hydroxylamine (HA), which cleaves the palmitate groups from cysteines that were then biotinylated using a thiol-reactive biotin molecule. As a negative control, the other half was not treated with HA (HA−). Subsequently, thiol-biotinylated proteins were purified by streptavidin beads (Fig. 4A). Palmitoylated proteins were expected to be present in the hydroxylamine-treated (HA+) eluates. Palmitoylation of PCDH7 was tested by western blotting

using an anti-PCDH7 antibody. In parallel, antibodies against EGFR and calnexin were used as positive controls that are known to be palmitoylated. Along with EGFR and calnexin, we observed PCDH7 in the palmitoylated fraction. As expected, PCDH7 was not detectable in the HA− fraction (Fig. 4B).

To further examine the palmitoylation of PCDH7, we used a standard palmitoylation inhibitor, 2-bromopalmitate (2BP), which is a non-metabolizable palmitate analog that inhibits the incorporation of palmitate into proteins (Webb et al., 2000). We first tested the effect of the palmitoylation inhibitor on the hydrophobicity of PCDH7 using Triton X-114 extraction, which separates proteins into detergent and aqueous phases according to their hydrophobic properties (Bordier, 1981). The inhibition of palmitoylation decreased the proportion of PCDH7 in the detergent phase, suggesting a reduction in the hydrophobicity of PCDH7 (Fig. S4A).

To examine the role of palmitoylation in mitosis-dependent PCDH7 cell surface localization, we tested the association of PCDH7 to the cell surface after palmitoylation inhibitor (2BP) treatment. For this, we purified cell surface proteins and compared PCDH7 levels in control and 2BP-treated cells. Briefly, HeLa S3 cells were treated with 2BP or DMSO (control) overnight, while being synchronized to interphase or mitosis using thymidine and STC, respectively. To enrich for cell surface-exposed proteins, intact cells were labeled with a non-permeable sulfo-NHS-SS-biotin reagent, followed by affinity purification of biotinylated proteins using streptavidin (Özkan Küçük et al., 2018). Although 2BP treatment did not affect biotinylated PCDH7 levels in interphase cells (Fig. 4C, left), it notably decreased the amount of biotinylated PCDH7 in mitotic cells [Fig. 4C, right, elute (E)] and increased the amount of unbiotinylated cytoplasmic PCDH7 [Fig. 4C, right, unbound (U)]. These results suggest that palmitoylation of PCDH7 is required for its mitotic cell surface localization. On the other hand, the amounts of EGFR in the input (I) and elute (E) lanes were comparable in both DMSO- and 2BP-treated cells, suggesting that during mitosis, this effect is specific to PCDH7.

To further examine the impact of the palmitoylation inhibitor on the subcellular localization of PCDH7 in mitotic and interphase cells, we performed immunostaining and live imaging of a PCDH7-GFP-BAC cell line treated with 2BP. In line with our previous findings (Fig. 4C), the inhibition of palmitoylation did not show a noticeable effect on the localization of PCDH7 at the cell–cell contacts during interphase (Fig. S4B). However, it significantly affected the surface localization of PCDH7 in mitotic cells (Fig. 5A) and decreased the plasma membrane enrichment (Fig. S4C) of PCDH7 (Fig. 5B). Live imaging of PCDH7 also supported these results (Fig. S4D; Movies 4 and 5).

To further investigate the effect of the palmitoylation inhibitor on the dynamic behavior of PCDH7 at the mitotic cell surface, we again took the FRAP approach and measured the extent of PCDH7::GFP recovery at the plasma membrane after photobleaching in the absence or presence of 2BP. Inhibition of palmitoylation did not have a significant effect on the FRAP recovery of PCDH7 at the cell–cell contacts during interphase (Fig. 5C, red and orange). On the other hand, 2BP treatment dramatically increased the FRAP recovery time of PCDH7 at the mitotic plasma membrane (Fig. 5C, dark blue and blue). These results suggest that inhibition of palmitoylation has a detectable effect on the dynamics of PCDH7 at the mitotic cortex but not at the cell–cell cortex.

Finally, we analyzed the effect of 2BP on the localization of PCDH7 during cytokinesis (Fig. 5D). Inhibition of palmitoylation explicitly perturbed the cleavage furrow and equatorial localization
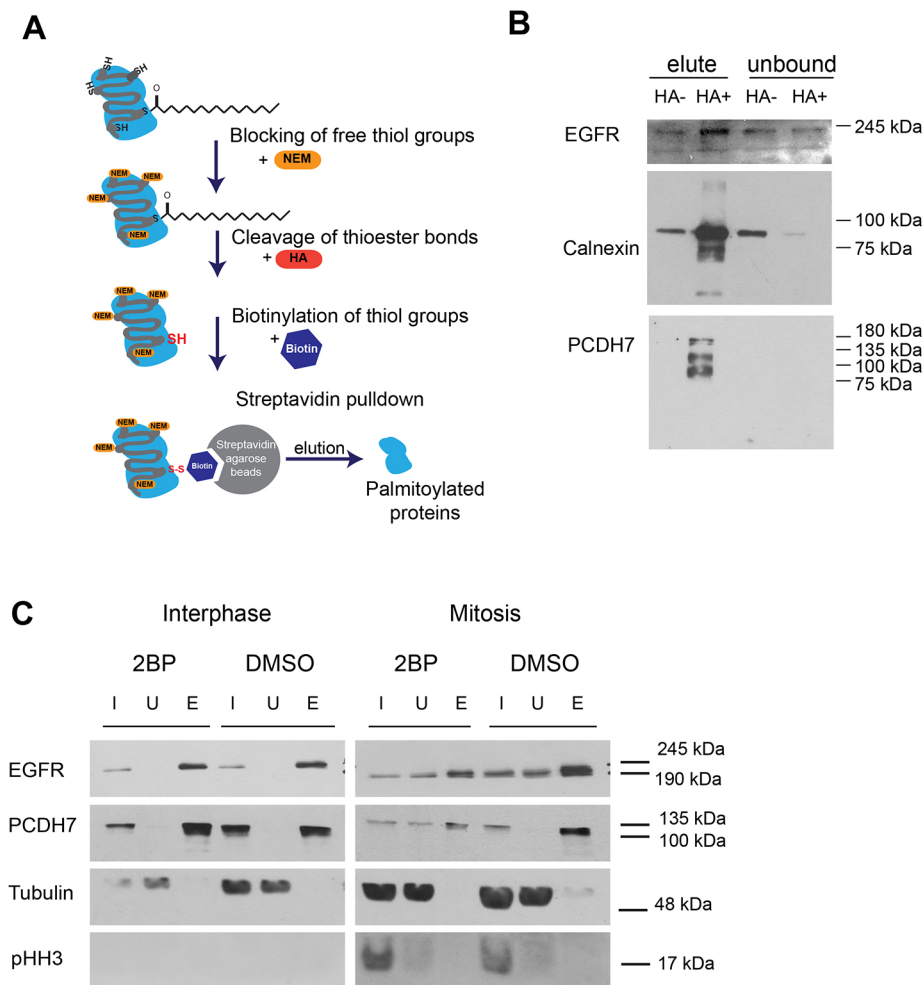
A

B

Fig. 4. PCDH7 is palmitoylated and palmitoylation is required for cell surface localization of PCDH7. (A) Schematic illustration of the acyl-biotin exchange (ABE) assay to identify palmitoylated proteins. N-ethylmaleimide (NEM) treatment blocks free thiols, whereas hydroxylamine (HA) treatment cleaves the palmitate groups from cysteine residues that are subsequently biotinylated with a thiol-reactive biotin molecule. Streptavidin pulldown was used to capture the palmitoylated proteins. (B) Western blot analyses of palmitoylated proteins after ABE assay. HA+ represents hydroxylamine-treated samples; HA− represents untreated ones. PCDH7::GFP-expressing HeLa S3 cells were used and PCDH7 was detected using anti-PCDH7 antibodies (PCDH7 is 116 kDa and PCDH7:: GFP is 143 kDa). Proteins that are known to be palmitoylated, namely EGFR and calnexin, were used as positive controls. (C) Western blot analyses of the effect of 2BP inhibitor treatment on cell surface localization of PCDH7. Surface-exposed proteins were labeled with non-permeable amine-reactive biotin and pulled down by streptavidin beads. All fractions (I, input; U, unbound; E, elute) were blotted using antibodies against EGFR (cell surface marker), PCDH7, α-tubulin (cytoplasmic marker) and phospho-histone H3 (pHH3) (mitotic marker). Images shown in B and C are are acquired from a single experiment; additional data in Fig. 5 and Fig. S4 supports these results.

C

of PCDH7 during cytokinesis (Fig. 5D; Fig. 5E, left) and led to a decrease in the levels of PCDH7 at the cleavage furrow (Fig. 5E, right). We conclude that palmitoylation is dispensable for stable localization of PCDH7 at cell–cell contacts during interphase, but essential for its cortical and cleavage furrow localization during mitosis and cytokinesis, respectively.

ZDHHC5-dependent palmitoylation directs PCDH7 to the plasma membrane at the onset of mitosis

Building upon the results of palmitoylation-dependent localization of PCDH7 in mitosis and cytokinesis, we next sought to examine the role of ZDHHC5 in this process. To this end, siRNA- (Fig. 6A) or shRNA- (Fig. S5A) mediated knockdowns of ZDHHC5 and control (non-targeting shRNA and siRNAs) HeLa PCDH7-GFP-BAC cells were used. In line with our previous observation, in control siRNA-treated cells, ZDHHC5 and PCDH7 largely colocalized at the mitotic cell surface and retraction fibers (Fig. 6B, top). Strikingly, ZDHCC5 depletion significantly decreased the PCDH7 signal at the mitotic cell surface (Fig. 6B, bottom; Fig. 6C). shRNA-mediated knockdown of ZDHHC5 (Fig. S5A) also gave similar results (Fig. S5B). The cell surface localization of PCDH7 during mitosis was significantly decreased upon shZDHHC5 treatment (Fig. S5B, right).

Next, we tested whether restoring ZDHHC5 expression could rescue impaired plasma membrane localization of PCDH7 during mitosis. Expression of murine ZDHHC5 in siZDHHC5 cells significantly restored the plasma membrane localization of

PCDH7 in mitotic cells. However, the catalytically inactive ZDHHC5 mutant C134S was not able to rescue this phenotype. PCDH7 levels at the plasma membrane were similar to those following siZDHHC5 treatment (Fig. 6D,E). These results indicate that the palmitoylation activity of ZDHHC5 translocates PCDH7 to the plasma membrane at the onset of mitosis.

ZDHHC5 directs PCDH7 to the cleavage furrow

Next, we examined the role of ZDHHC5 in targeting PCDH7 to the cleavage furrow. In ZDHHC5-depleted cells, cleavage furrow localization of PCDH7 was perturbed (Fig. 7A,B). PCDH7 was no longer enriched at the cleavage furrow or the equatorial zone during late cytokinesis in ZDHHC5 knockdown cells (Fig. 7A,B).

As ZDHHC5 localizes to the cleavage furrow together with PCDH7, we next examined whether ZDHHC5 depletion affected cytokinesis. Intriguingly, we observed a significantly increased multinucleation rate (8.5%) in shZDHHC5 cells in comparison to that in cells treated with control shRNA (4.6%) (Fig. S5C; Fig. 7C). To conclude, ZDHHC5 localizes and targets PCDH7 to the cleavage furrow and equatorial zone during cytokinesis.

Lack of PCDH7 at the cleavage furrow diminishes phospho-myosin levels at the contractile ring

To gain more insight into the cytokinesis defect of PCDH7-depleted cells, we monitored active RhoA and myosin levels at the cleavage furrow. Control and PCDH7 KO cells were transfected with an eGFP–RhoA Biosensor (Piekny and Glotzer, 2008) that binds only
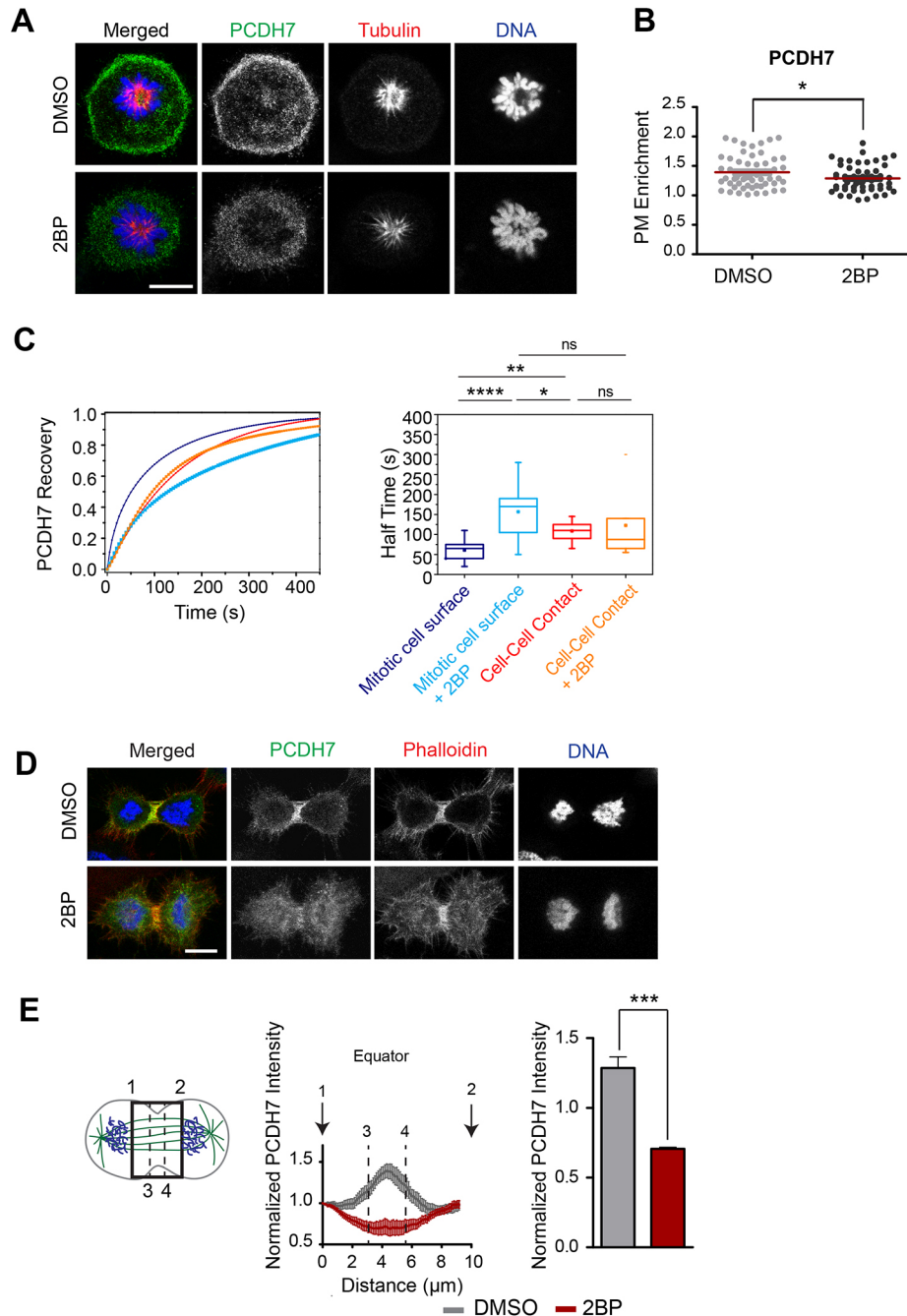
Fig. 5. Inhibition of palmitoylation perturbs cell surface and cleavage furrow localization of PCDH7. (A) PCDH7 (green, anti-GFP) localization during mitosis in control (DMSO) (top) and palmitoylation inhibitor (2BP)-treated (bottom) cells stably expressing PCDH7-GFP-BAC. Cells were synchronized to monopolar mitosis. Microtubules (anti-β-tubulin) are shown in red and DNA (DAPI) in blue. Plasma membrane enrichment scores for the representative images are 1.72 for the control cell and 1.16 for the 2BP-treated one. (B) Quantification of the plasma membrane (PM) enrichment of PCDH7 in the control (n=56) and 2BP-treated (n=54) mitotic cells. Mean values for plasma membrane enrichment scores are 1.39 and 1.28 for control and 2BP-treated cells, respectively. Statistical analyses used unpaired two-tailed t-test. (C) FRAP analysis of PCDH7 in 2BP-treated cells. Recovery curves (left) of PCDH7 on the mitotic cell surface (dark blue) (n=23 cells), 2BP-treated mitotic cell surface (light blue) (n=9 cells), cell–cell contact regions (red) (n=25 cells) and 2BP-treated cell–cell contact regions (orange) (n=6 cells) after photobleaching. Comparison of recovery halftimes in control and 2BP-treated cells (right). Boxes show the 25–75th percentiles, whiskers represent the minimum and maximum values, and the median is marked with a line. Statistical analyses used one-way ANOVA with Tukey's multiple comparison test. (D) PCDH7 (green, anti-GFP) localization at the equatorial zone during cytokinesis in control (top) and 2BP-treated (bottom) PCDH7-GFP-BAC-expressing cells. Each image is the maximum-intensity projection of a z-stack. Actin filaments (phalloidin) are shown in red and DNA (DAPI) in blue. (E) Illustration of the analyzed region of interest in the cell (left). Intensity profiles (measured from 1 to 2) (middle) of PCDH7 in the control (n=13 cells) (gray) and 2BP-treated (n=26 cells) (red) cytokinetic cells. The sum of PCDH7 intensities between the dashed lines covering the ±15% distance around the middle zone (measured from 3 to 4) was quantified (right). Intensity profiles were obtained using ImageJ software for the indicated region of interest as previously described (Uretmen Kagiali et al., 2020). Statistical analyses used unpaired two-tailed t-test. Error bars show the s.d. ns, not significant; *P<0.05; **P<0.01; ***P<0.001; ****P<0.0001. Scale bars: 10 μm.
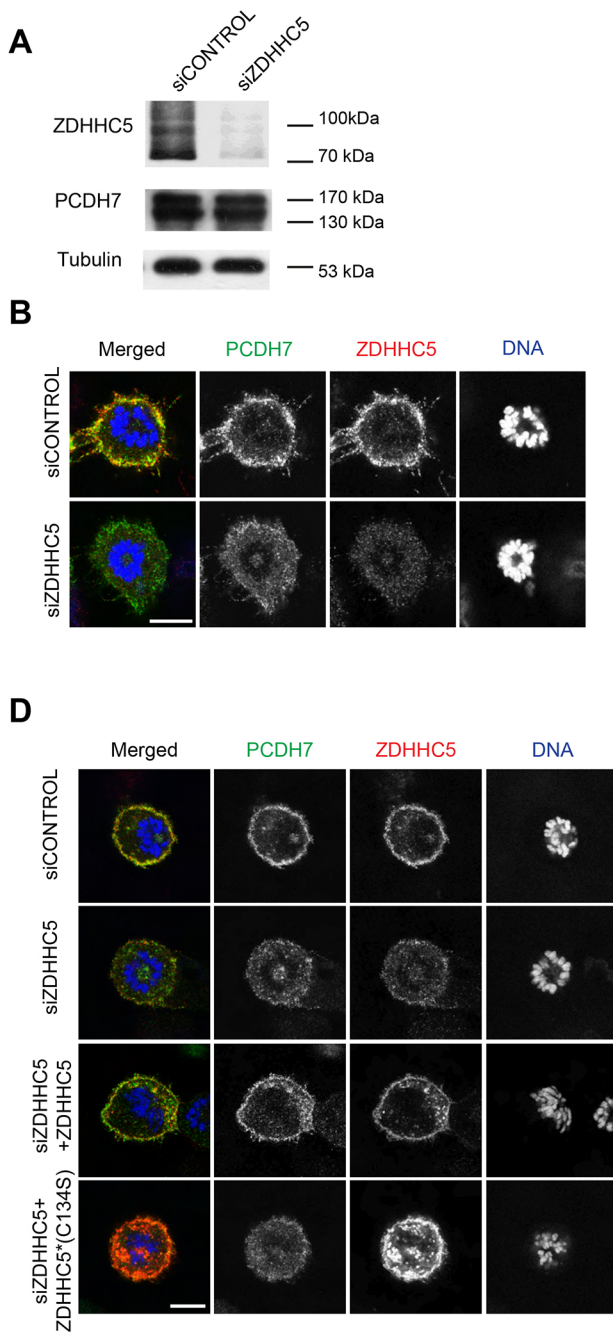
Fig. 6. ZDHH5 targets PCDH7 to the plasma membrane during mitosis. (A) Western blotting analysis of siZDHHC5 and siCONTROL cells. siZDHHC5 treatment successfully depleted the ZDHHC5 proteins, whereas PCDH7 levels remained unchanged. α-tubulin was used as the loading control. (B) PCDH7 (green, anti-GFP) localization in mitotic control (siCONTROL) (top) and ZDHHC5 knockdown (siZDHHC5) (bottom) cells stably expressing PCDH7-GFP-BAC. Cells were synchronized to monopolar mitosis. ZDHHC5 is shown in red (anti-ZDHHC5) and DNA in blue (DAPI). (C) Quantification of the plasma membrane enrichment of PCDH7 during mitosis in control (n=39) and ZDHHC5 knockdown (n=83) cells (right). Statistical analyses used unpaired two-tailed t-test. (D) PCDH7 (green, anti-GFP) localization in mitotic control (siCONTROL), ZDHHC5 knockdown (siZDHHC5) and ZDHHC5-rescued cells that were stably expressing PCDH7-GFP-BAC. To restore ZDHHC5 expression, cells were transfected with either wild-type ZDHHC5 or the catalytically inactive mutant [ZDHHC5*(C134S)]. (E) Quantification of the plasma membrane enrichment of PCDH7 during mitosis in the control (n=10) and ZDHHC5 knockdown (n=10), ZDHHC5-transfected (n=6), and ZDHHC5 mutant (C134S)-transfected (n=8) cells (right). Statistical analyses used one-way ANOVA with Bonferonni's multiple comparison test. Error bars show the s.e.m. ns, not significant; *$P<0.05$; **$P<0.01$; ***$P<0.001$. Scale bars: 10 μm.

to the active form of RhoA, enabling tracking of RhoA activity. Live-cell imaging was performed to compare RhoA activity during cytokinesis in control (Fig. 8A, top; Movie 6) and PCDH7 KO (Fig. 8A, bottom; Movie 7) cells. Active RhoA levels at the cleavage furrow were significantly decreased in PCDH7 KO cells compared with those in the control cells (Fig. 8B; Fig. S5). Although active RhoA levels were impaired, the cells were able to initiate furrow ingression in PCDH7 KO cells. However, a significant portion of those cells (11.7%) failed to complete furrow ingression and they merged back (Fig. S6B,C).

Next, we examined active myosin levels in PCDH7-depleted cells by using an anti-phospho-myosin II (S19) antibody (Matsumura et al., 1998) (Fig. 8C). The phosphorylated myosin was significantly enriched at the cleavage furrow in control cells (Fig. 8D, gray). In PCDH7 KO cells,

phospho-myosin intensity was significantly reduced at the cleavage furrow (Fig. 8D, red). The expression of ectopic PCDH7 in PCDH7 KO cells significantly replenished the phospho-myosin levels (Fig. 8D, blue).

In agreement with ZDHHC5 dependency of PCDH7, similar to PCDH7, depletion of ZDHHC5 caused a significant decrease in phospho-myosin (S19) levels at the cleavage furrow (Fig. 8E,F). Taken together, our data suggest that the ZDHHC5–PCDH7 axis has an impact on RhoA and myosin activity during cytokinesis, thus contributing to the fidelity of cell division.

DISCUSSION
This study aimed to understand the function and the underlying mechanism of cell cycle-dependent localization of PCDH7. Our analysis revealed an unprecedented role of palmitoylation in the
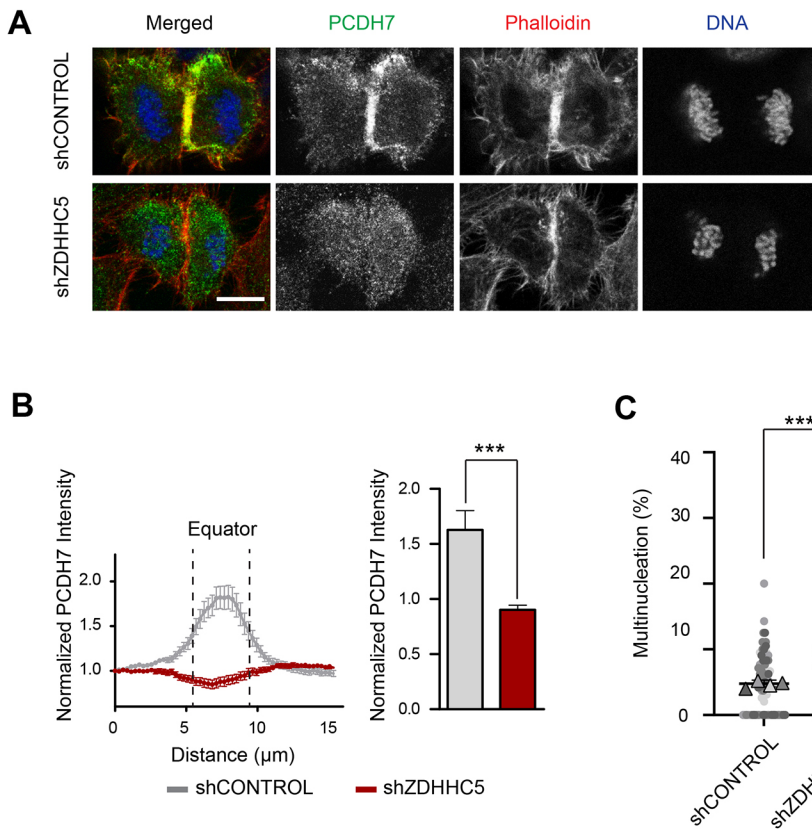
Fig. 7. ZDHHC5 targets PCDH7 to the equatorial zone between segregating chromosomes and contributes to cytokinesis. (A) Representative maximum-intensity projections of z-stacks show PCDH7 (green, anti-GFP) localization at the equatorial zone during cytokinesis in shCONTROL (top) and shZDHHC5 (bottom)-treated PCDH7-GFP-BAC cells. Actin filaments (phalloidin) are shown in red and DNA (DAPI) in blue. Scale bar: 10 μm. (B) Intensity profiles of PCDH7 in the control (gray) (n=35) and ZDHHC5 knockdown (red) (n=43) cells (left). The sum of PCDH7 intensities between the dashed lines covering the ±15% distance around the middle zone was quantified (right). Intensity profiles were obtained in ImageJ software for the indicated region of interest as previously described (Uretmen Kagiali et al., 2020). Statistical analyses used unpaired two-tailed t-test. Error bars show the s.d. (C) Quantification of multinucleation percentages of control (gray; mean 4.79%, n=1415) and ZDHHC5 knockdown (red; mean 9.429%, n=1276) cells. An average of 24 fields were scored for each group. Data are represented as individual percentages for each field (colored circles) and average percentages for each independent biological replicate (colored triangles). Statistical analyses used logistic regression analysis followed by P-value adjustment with the Bonferroni method. The mean with s.e.m. for each group is represented with black lines. ***P<0.001.

translocation of PCDH7 to the mitotic cell surface and cleavage furrow, which promotes myosin phosphorylation at the cleavage furrow. Palmitoylation is a reversible post-translational modification that plays a key role in controlling protein targeting by increasing the hydrophobicity of a protein (Linder and Deschenes, 2007). Our data support a mechanism by which palmitoylation of PCDH7 stabilizes its cell surface and cleavage furrow localization. Indeed, its cell surface and cleavage furrow localization during mitosis and cytokinesis, respectively, was dependent on palmitoylation, whereas the localization to cell–cell contacts during interphase was not affected by palmitoylation inhibition. Our FRAP analysis revealed that the turnover rate and dynamics of molecules at the cell–cell contact region and cell surface are different: they are faster at the cell surface during mitosis. It is possible that trans interactions are more stable and palmitoylation is dispensable or less critical for trans-clustered molecules at the cell–cell contact regions. Our analysis revealed that PCDH7 is palmitoylated; however, our attempts at finding palmitoylation sites by mutating potential cysteine residues that affect protein localization failed. It is challenging to determine palmitoylation sites because of the lack of a consensus motif. Besides cysteine, palmitoylation can also occur on serine and lysine residues. In addition, a cumulative effect of palmitoylation on multiple cysteines and even on serine or lysine (Brownlee and Heald, 2019) residues might be involved; thus, mutating individual residues might not be sufficient to mimic the unpalmitoylated form. Similarly, PCDH1, which shares 46% homology with PCDH7, was also found to be palmitoylated and localized to the membrane in a palmitoylation-dependent manner (Kahr et al., 2013). However, mutating one palmitoylated cysteine residue was not sufficient to mimic treatment with the palmitoylation inhibitor and exhibit the membrane localization phenotype (Kahr et al., 2013). More work is

required to understand the molecular details in the palmitoylation of non-clustered protocadherins.

Our BioID-based proximity interactome identified the palmitoyl transferase ZDHHC5 as a significant interactor of PCDH7. In contrast to the majority of palmitoyl acyl transferases that localize to the Golgi or endoplasmic reticulum, ZDHHC5 localizes to the plasma membrane (Ohno et al., 2006). ZDHHC5 has been implicated in multiple cellular processes such as endocytosis, cell adhesion, Na$^+$ pump activity and pathogen–host interactions, partly by regulating the localization of related proteins (Plain et al., 2020; Pradhan et al., 2021; Woodley and Collins, 2019, 2021). In this study, for the first time, we analyzed the function of ZDHHC5 in the context of cell division. At metaphase, ZDHHC5 localizes to the mitotic cell surface and retraction fibers, and it concentrates at the cleavage furrow during cytokinesis. The translocation of PCDH7 to the mitotic cortex and cleavage furrow occurs in a ZDHHC5 palmitoylation activity-dependent manner.

Loss of ZDHHC5 caused cytokinesis defects and a statistically significant increase in the rate of multinucleated cells. Imaging of protein fatty acylation in cells undergoing cell division has revealed that at metaphase, S-palmitoylation is enriched at the cell surface and around the spindle, and as cells progress into cytokinesis, palmitoylated proteins are concentrated at the cleavage furrow (Hannoush and Arenas-Ramirez, 2009). Based on those findings, it is entirely possible that palmitoyl acyl transferases, and in part ZDHHC5, might have a wider role in organizing the mitotic cell cortex and targeting cell division-related proteins to the plasma membrane and cleavage furrow. PCDH7 might be the very first example of many cell cycle-dependent palmitoylated proteins. Although many studies have indicated the role of protein palmitoylation in protein trafficking (Linder and Deschenes, 2007) and different intracellular signaling pathways (Resh, 2006),
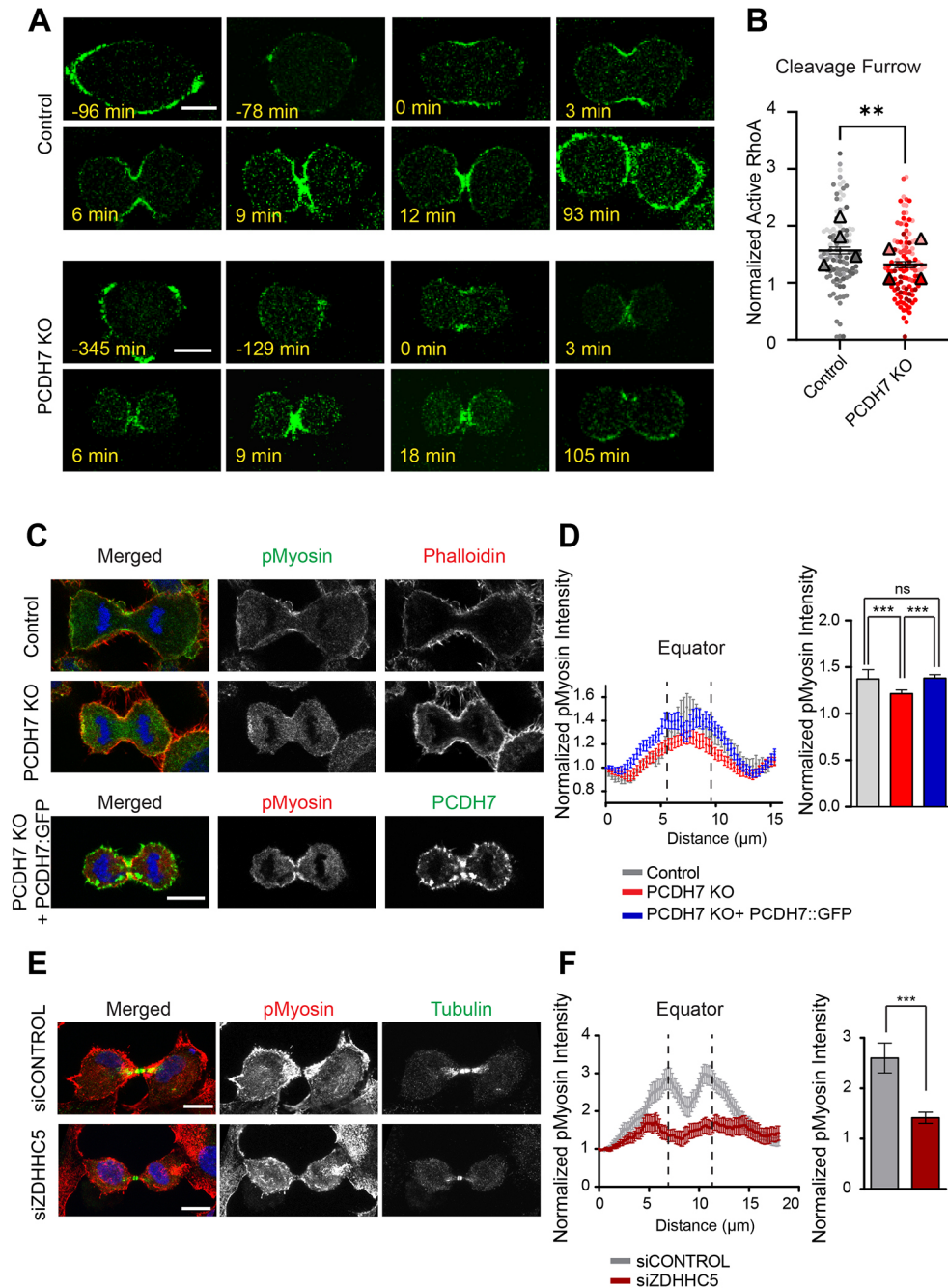
Fig. 8. Active RhoA and myosin phosphorylation levels are diminished at the cleavage furrow in PCDH7-depleted cells. (A) Live-imaging snapshots of control and PCDH7 knockout (KO) cells that were transfected with a pEGFP–RhoA biosensor vector to track active RhoA. The relative timing to cleavage furrow ingression is shown in minutes. (B) Quantification of the active RhoA levels at the cleavage furrow in control (gray) and PCDH7 KO (red) cells. Data are represented as individual values for each of four independent biological replicates (BR) [control, n=28 (BR1), n=10 (BR2), n=47 (BR3) or and n=27 (BR4) cells; PCDH7 KO, n=23 (BR1), n=22 (BR2), n=49 (BR3) or and n=21 (BR4) cells] (colored circles) and average values for each group (colored triangles). The detail of the quantification method is illustrated in Fig. S6. Statistical analyses used unpaired two-tailed t-test. Mean with s.e.m. for each group is represented with black lines. (C) Representative fluorescence images displaying phospho-myosin II (S19) (pMyosin, green), actin filaments (red, phalloidin), and DNA (blue, DAPI) localization in control (top) and PCDH7 KO (middle) cells. Representative images of a rescued cell (PCDH7 KO+PCDH7::GFP, bottom) show PCDH7::GFP (green), phospho-myosin II (S19) (red) and DNA (blue, DAPI). (D) Intensity profiles of pMyosin levels at the equatorial zone during cytokinesis in the control (gray) (n=24), PCDH7 KO (red) (n=24), and rescued (PCDH7 KO+PCDH7::GFP) (blue) (n=41) cells (left). The sum of pMyosin intensities between the dashed lines covering the ±15% distance around the middle zone was quantified (right). Statistical analyses used one-way ANOVA with Bonferonni's multiple comparison test. Error bars show the s.d. (E) Representative fluorescence images displaying phospho-myosin II (S19) (red), microtubules (green, anti-β-tubulin) and DNA (blue, DAPI) localization in control (top) and ZDHHC5 knockdown (bottom) cells at cytokinesis. Maximum-intensity projections of z-stacks are shown. (F) Intensity profiles of pMyosin levels at the equatorial zone during cytokinesis in the control (gray) (n=28) and ZDHHC5 knockdown (red) (n=23) cells (left). The sum of pMyosin intensities between the dashed lines covering the ±15% distance around the middle zone was quantified (right). Statistical analyses used unpaired two-tailed t-test. Error bars show the s.d. ns, not significant; **P<0.01; ***P<0.001. Scale bars: 10 µm.

the importance of palmitoylation in the context of cell division has been emerging only recently. Depalmitoylation activity is required for the unequal partitioning of Notch and Wnt signaling during asymmetric cell division (Stypulkowski et al., 2018). Palmitoylation-dependent membrane association of importin α has been shown to affect the mitotic spindle and nuclear scaling during *Xenopus* embryogenesis (Brownlee and Heald, 2019). Our findings attribute new functional aspects to the role of palmitoylation in cell division. Future studies will expand upon the palmitoylation-dependent regulatory mechanisms during cell division by investigating palmitoyltransferases and their target molecules that function in mitosis and cytokinesis.

What is the function of PCDH7 during cell division? Our previous study showed that PCDH7 is required for the development of full mitotic rounding pressure (Ozlu et al., 2015). Rounding pressure is dependent on myosin II activity (Stewart et al., 2011a,b). In the present study, we have shown that the knockout of PCDH7 caused a statistically significant increase in cytokinesis failure in HeLa S3 cells and a delay in mitosis. One possible explanation for the increased duration of mitosis in PCDH7-depleted cells is that rounding pressure that is regulated by PCDH7 is needed for the accurate timing of mitosis.

The multinucleation phenotype caused by PCDH7 depletion was moderate but significant. In our previous study, although we observed a reduced rounding pressure in PCDH7 siRNA cells, the cells were still able to round up. The weakness of the observed phenotypes might be due to the functional redundancy between PCDH1 and PCDH7 and the fact that multiple parallel pathways act together for mitotic rounding and cytokinesis (Cramer et al., 1994; Ramkumar and Baum, 2016). We observed that RNAi-based depletion of PCDH7 in HeLa Kyoto and HEK293T cells induces a higher multinucleation rate than CRISPR-based knockout of PCDH7 in HeLa S3 cells. The stronger phenotype observed in RNAi experiments might be because PCDH7 KO cells might have developed compensatory changes in the absence of PCDH7 and such adaptations were not developed in acute depletions. Besides, HeLa Kyoto cells and HEK293T cells are more adherent than HeLa S3 cells and this suggests that adherent cells are affected more by the depletion of PCDH7.

In addition, we observed that PCDH7 accumulates asymmetrically at the cleavage furrow. PCDH7 might have a role in apical-basal polarity and its major impact in cytokinesis might only be evident in the epithelium where cells are tightly packed and polarized, and not when cells are grown separately in culture. True epithelial cells in culture and three-dimensional cultures should be used in future studies to circumvent this issue.

The actomyosin network is important for mitotic rounding and cleavage furrow formation, and both processes appear to be affected in the absence of PCDH7. A previous genome-wide RNAi screen also reported binucleation and cell migration defects in PCDH7-depleted cells (Neumann et al., 2010). Indeed, we observed that active RhoA and myosin levels at the cleavage furrow were significantly reduced in the absence of PCDH7 when compared to the control cells. Previously it was reported that PCDH7 increases phospho-myosin light chain levels to enhance anchorage-independent cell growth (Wang et al., 2020). Similarly, in a parallel study, we observed that PCDH7 overexpression enhances phospho-myosin levels during cell migration in Retinal Pigment Epithelial (RPE) cells and PCDH7 interacts with PP1cβ, the catalytic subunit, and MYPT1, the myosin targeting subunit of myosin phosphatase (Qureshi et al., 2022 preprint). Previous studies also reported that PCDH7 behaves as a signaling molecule more than an adhesion molecule and inhibits the phosphatase activities of

PP1aa and PP2A (Wang et al., 2020; Zhou et al., 2017). Recently, it has been reported that PCDH7 functions in osteoclast differentiation by regulating RhoA and Rac1. Loss of PCDH7 expression impairs RhoA activation in pre-osteoclasts (Kim et al., 2021). In agreement with those studies, we also observed that depletion of PCDH7 impairs active RhoA and myosin levels at the cleavage furrow, albeit RhoA and myosin activity were sufficient for promoting actomyosin ring constriction and furrow ingression. Instead, we observed defects in the completion of furrow ingression and higher rates of merged cells upon PCDH7 depletion. Further studies are necessary to elucidate the molecular details of PCDH7-dependent regulation of the actomyosin cortex and the association of PCDH7 expression with RhoA and myosin activity during cytokinesis.

In summary, our study suggests a new pathway for cell cycle-dependent protein localization during cell division. We suggest that ZDHHC5-dependent targeting of PCDH7 to the cell cortex and cleavage furrow contributes to cortical remodeling. The molecular details of palmitoylation-dependent cortical regulation during cell division will unravel the fundamental redundant pathways existing in human cells.

MATERIALS AND METHODS
Cell lines and culture
HeLa S3 (American Type Culture Collection, CCL-2.2, female), HeLa Kyoto (a gift from Ulrike Eggert, Randall Centre for Cell and Molecular Biophysics, School of Basic and Medical Biosciences, King's College London, London, UK), and HEK293T [a gift from Dr Tamer Önder, Koç University Research Center for Translational Medicine (KUTTAM), Istanbul, Türkiye., Koç University School of Medicine, Istanbul, Türkiye] cells were grown in Dulbecco's modified Eagle medium (DMEM) (Sigma-Aldrich, D6429) supplemented with 1% penicillin-streptomycin (P/S) (Capricorn Scientific, PS-B) and 10% fetal bovine serum (FBS) (Gibco, 10270106). The PCDH7-GFP-BAC (Poser et al., 2008) transgenic cell line was a kind gift from Dr Ina Poser (Max Planck Institute of Molecular Cell Biology and Genetics, Dresden, Germany) and was grown in DMEM supplemented with 1% P/S, 10% FBS and 400 µg/ml G418 (Santa Cruz Biotechnology, sc-29065A). HeLa S3 cells stably expressing PCDH7::GFP were created by lentiviral delivery of the PCDH7::GFP construct, acquired by cloning PCDH7 into the pLenti CMV GFP Puro (pLenti) (Addgene, 17448) mammalian expression vector, and were grown in DMEM supplemented with 1% P/S, 10% FBS, and 2 µg/ml puromycin. To inhibit palmitoylation, cells were incubated with 100 µM 2BP (Sigma-Aldrich, 21604) overnight (Webb et al., 2000).

Cell synchronization
Cells synchronization to interphase, mitosis (Ozlü et al., 2010) and cytokinesis (Hu et al., 2008; Karayel et al., 2018) was performed as previously described. Cells were synchronized to interphase by a double thymidine block using 2 mM thymidine (Santa Cruz Biotechnology, sc-296542). Subsequently, to induce monopolar mitosis, cells were treated with 10 µM S-trityl-L-cysteine (STC) (Sigma-Aldrich, 164739). For synchronization of monopolar cytokinesis, cells were treated with 10 µM STC and then 100 µM purvalanol A (Tocris Bioscience, 1580). For synchronization of bipolar cytokinesis, cells were incubated with 10 ng/ml of nocodazole (Calbiochem, 487928) for 5 h for mitosis and released from nocodazole for 1 h for cytokinesis.

Immunostaining and microscopy
For immunostaining, cells were plated on coverslips (12 mm), fixed with 3% paraformaldehyde, blocked, and incubated with primary and secondary antibodies in 2% bovine serum albumin (BSA) in PBS containing 0.1% Triton X-100. The following antibodies and reagents were used: anti-β-tubulin (Cell Signaling Technology, CS2128S, 1:500), anti-α-tubulin (Cell Signaling Technology, 3873S, 1:1000), anti-tubulin (Abcam, ab6160, 1:500), anti-GFP (non-commercial antibody, 1:5000; Invitrogen, A11120,

1:1000), anti-HA (Abcam, ab16918, 1:200), anti-phospho-myosin (Cell Signaling Technology, CS3675, 1:500), anti-ZDHHC5 (Atlas Antibodies, HPA014670, 1:500), Alexa Fluor 488 (Invitrogen, A21202, A21206, 35552, 1:1000)- and Alexa Fluor 555 (Invitrogen, A11077, 1:1000) conjugated secondary antibodies, Streptavidin–Alexa Fluor 488 (Invitrogen, S32354, 1:1000), Phalloidin iFluor 555 (Abcam, ab176756, 1:1000) and DAPI (Sigma-Aldrich, D8417).

For live imaging, ibiTreat µ-Slide 8 Well (ibidi, 80826) or µ-Dish 35 mm (ibidi, 81156) plates were used. Confocal microscopy was performed with a Leica DMi8/SP8 TCS-DLS (LAS X Software) laser scanning confocal microscope using 40× Plan Apo 1.3 NA and 63× Plan Apo 1.4 NA oil-immersion objectives. Live-imaging experiments were performed using a Leica DMi8 widefield fluorescence microscope (LAS X Software) or Leica DMi8/SP8 TCS-DLS confocal microscope equipped with 37°C and 5% CO_2 chambers. 63× Plan Apo 1.4 NA oil-immersion or 20× PL FLUOTAR L 0.40 NA objectives were used. Single images or z-stacks were acquired every 3 min and a single focal plane was used in the figures unless specified in the figure legends.

Apart from FRAP data, all images were analyzed in Fiji. Graphs and statistical data were generated in GraphPad Prism, except for multinucleation data. Statistical tests for multinucleation analysis were performed in R: to test the significance of changes in the proportion of 'normal' cells across conditions, we reformulated the 2×2 contingency tables as data tables suitable for logistic regression analysis. We applied the Bonferroni test. Specifically, we used the glm function in R with family='binomial' option to test the changes in the log odds ratio of 'normal' cells given the condition. We used the replicate of the origin of each cell as a covariate term for the logistic regression model. Finally, we used the 'p.adjust' function with the method='bonferroni' option to adjust P-values from coefficients of multiple logistic regression models. Statistical details of each experiment including the statistical test used, the exact value of n and definition of error bars are given in the figure legend for each figure.

FRAP analysis
Microscopy setup
The microscopy setup included a frequency-doubled femtosecond-pulsed Ti:Sa solid-state tunable laser source (Chameleon Ultra II, Coherent) equipped with a second harmonic generator. The laser output was tuned to 488 nm and the beam was directed through mirrors and a Keplerian telescope to the inverted microscope (Eclipse TE2000-U; Nikon) equipped with a dichroic mirror (Chroma, Q495LP) and 60× oil-immersion objective (Nikon Apo TIRF, NA 1.49). A 300 mm focal length lens was placed right before the microscope to focus the laser at the back focal plane of the microscope objective to obtain widefield illumination. The microscope was equipped with two different cameras for brightfield and fluorescence image acquisitions. Brightfield images were captured by a CCD camera (Thorlabs, DCU223M). Fluorescence images were captured by an EMCCD camera (Hamamatsu ImagEM C9100-13) placed after an emission filter with a pass band of 530±30 nm. Photobleaching was performed by removing the neutral density optical filter and the lens right before the microscope, and simultaneously focusing the laser light at the desired area for 1 s. FRAP image acquisition was done every 5 s using an automated shutter and a minimum of 130 frames were captured following the photobleaching of each sample.

Data processing
Image analysis was done by using a MATLAB code based on the double-normalization algorithm (Phair et al., 2004). The code for FRAP analysis is available at https://github.com/nbavili/FRAP/blob/main/FRAP_MATLAB_CODE.m. In this method, the overall decrease in the fluorescence intensity of the samples is also considered and the normalized intensity of the ROI ($I_{normalized}$) is given by:

$$I_{normalized}(t) = \frac{I_{total,prebleached} - BG}{I_{bleached\ region,prebleached} - BG} \cdot \frac{I_{bleached\ region}(t) - BG}{I_{total}(t) - BG},$$

where $I_{total,prebleached}$ and $I_{bleached\ region,prebleached}$ are prebleached intensities of the whole cell and the ROI, respectively. $I_{bleached\ region}(t)$ and $I_{total}(t)$ are

corresponding intensities at time t. BG is the intensity of the background region. The total number of frames and the first post-bleached frame were defined for each sample. The size of the selected background and the ROI areas in each sample was fixed to 14×14 pixels (Kappel and Eils, 2004). Unhealthy cells and motile cells that obstructed the ROI tracking throughout the frames were excluded from the data. The obtained $I_{normalized}(t)$ data for each cell then were fitted to $1 - Ae^{-at} - Be^{-bt}$ (Phair et al., 2004) to get half time values $t_{1/2}$. The recovery percentage was also calculated for each cell. The Mann–Whitney U-test was applied to reveal statistical differences in the recovery and the half-time between samples. Average recovery curves for each group of cells (cell–cell contacts in interphase and mitotic plasma membrane) were obtained by normalizing all individual recovery graphs recorded within a group to 1 and calculating the average points as well as standard deviations of the recovery data at specified frames (time instances) after photobleaching.

Transfection and viral transduction
Cells were transfected using polyethylenimine (PEI) (Polysciences, 23966), Lipofectamine 2000 (Invitrogen, 11668019) or Lipofectamine RNAiMAX (Thermo Fisher Scientific, 13778075) protocols. For the PEI protocol, transfection mixtures were prepared in Opti-MEM reduced serum medium (Invitrogen, 31985047) using PEI with 60 µg DNA/150 mm dishes in a 3:1 ratio. After 30 min of incubation at room temperature, the transfection mixture was added to the cells. For the Lipofectamine 2000 protocol, the manufacturer's instructions were followed.

Plasmids encoding murine ZDHHC5 and its catalytically inactive mutant ZDHHC5 (C134S) were kindly provided by Prof. William Fuller (Institute of Cardiovascular and Medical Sciences, College of Medical, Veterinary and Life Sciences, University of Glasgow, UK). The pEGFP-RhoA Biosensor plasmid was acquired through Addgene (#68026).

For viral transduction, lentiviruses were packaged in HEK293T cells using PEI transfection of the target sequence-containing vector (pLenti), packaging vector (psPAX2, Addgene #12260) and envelope vector (pCMV-VSV-G, Addgene #8454). Viral particles were collected after 48 and 72 h of transfection and used to infect HeLa S3 in the presence of 2 µg/ml protamine sulfate (Sigma-Aldrich, P4505) as a coadjutant. Transduced cells were then selected with the appropriate selective antibiotic.

Identification of proximity-dependent interactions
The PCDH7 sequence was amplified from the PCDH7::eGFPN1 construct (Ozlu et al., 2015) using specific primers (5′-GTCAGCTAGCACC-ATGCTGAGGATGCGGACC-3′ and 5′-GCTAGAATTCGCCCTCCC-TGGGATATTTAAATATATTTG-3′) and cloned into the BioID vector [pcDNA3.1 MCS-BirA* (R118G)-HA, Addgene #36047].

Proximity-dependent biotinylation was performed as previously described (Roux et al., 2012). Briefly, cells were transfected with the BioID vector and incubated with 50 µM biotin (Invitrogen, B20656) during interphase and mitosis synchronization. Cell pellets were lysed in lysis buffer [50 mM Tris-HCl, pH 7.4; 500 mM NaCl; 0.4% SDS; 5 mM EDTA; 2% Triton X-100; 1 mM dithiothreitol (DTT; Sigma-Aldrich, 43815); and protease inhibitor] and incubated with streptavidin beads (Pierce, 53117) overnight at 4°C in a tube rotator. Whole-cell lysates and unbound fractions were kept at −20°C for further analysis. Beads were washed with wash buffer 1 (2% SDS in dH_2O), wash buffer 2 (2% deoxycholate; 1% Triton X-100; 50 mM NaCl; 50 mM HEPES, pH 7.5; and 1 mM EDTA), wash buffer 3 (0.5% NP-40; 0.5% deoxycholate; 1% Triton X-100; 500 mM NaCl; 1 mM EDTA; and 10 mM Tris, pH 8.1) and wash buffer 4 (50 mM Tris, pH 7.4; 50 mM NaCl) sequentially. For western blotting analysis, bound proteins were eluted from the streptavidin beads with 50 µl of Laemmli-DTT sample buffer containing 500 nM D-biotin (Invitrogen, B1595) at 98°C by shaking at 1000 rpm in a ThermoMixer (Eppendorf). For mass spectrometry analysis, on-bead tryptic digestion was performed. Briefly, beads were washed with urea buffer [8 M urea (Sigma-Aldrich, A2383); 0.1 M Tris-HCl, pH 8.5]. Then, bead-bounded proteins were reduced with 100 mM DTT and alkylated using 100 mM iodoacetamide (AppliChem, A1666). After alkylation, beads were washed with 50 mM ammonium bicarbonate (AppliChem, A3583) and incubated with trypsin (Thermo Fisher Scientific, 25247) at 37°C overnight (14–16 h) in the ThermoMixer.

The resulting digested peptides were collected and desalted using C18 STAGE tips (Rappsilber et al., 2007). The experiment was performed in four biological replicates with a minimum of two technical replicates for each condition.

Mass spectrometry and data analysis

Peptides were analyzed by online C18 nanoflow reversed-phase nLC (NanoLC-II, Thermo Fisher Scientific) or C18 nanoflow reversed-phase HPLC (Dionex Ultimate 3000, 3500 RSLC nano, Thermo Fisher Scientific) connected with an orbitrap mass spectrometer (Q Exactive Orbitrap, Thermo Fisher Scientific). Samples were separated in an in-house packed 100 µm (internal diameter)×23 cm C18 column (Reprosil-Gold C18, 5 µm, 200 Å, Dr. Maisch) using 80-min linear gradients from 5–25%, 25–40% and 40–95% acetonitrile in 0.1% formic acid with 300 nl/min flow in 100 min total run time. The scan sequence began with an MS1 spectrum [Orbitrap analysis; resolution 70,000; mass range 400–1500 m/z; automatic gain control (AGC) target 1e6; maximum injection time 32 ms]. Up to 15 of the most intense ions per cycle were fragmented and analyzed in the orbitrap with data-dependent acquisition. MS2 analysis consisted of collision-induced dissociation (higher-energy collisional dissociation) (resolution 17,500; AGC 1e6; normalized collision energy 26; maximum injection time 85 ms). The isolation window for MS/MS was 2.0 m/z.

Raw files were processed with the Proteome Discoverer 2.3 (Thermo Fisher Scientific) software. Carbamidomethylation of cysteine residues was used as a fixed modification, and acetylation (of protein N-termini) and oxidation of methionine residues were used as variable modifications. A maximum of two missed cleavages was allowed for the tryptic peptides. The precursor mass tolerance was set to 10 parts per million and fragment mass tolerance was set to 0.02 Da. Both peptide and protein FDRs were set to 0.01. The other parameters were used with default settings. The database search was performed against the human UniProt database (release 2015) containing 21,039 entries using the SEQUEST HT search engine integrated into the Proteome Discoverer environment.

Network analysis

The spectral counts of proteins were used to calculate fold-change ratios and FDR values for identified proteins using the qspec-param program of qprot_v1.3.5 (Choi et al., 2015). Proteins were filtered with a 0.05 cut-off for FDR values. Significant protein hits were loaded into the STRING database v11.0 (Szklarczyk et al., 2019) using the Cytoscape StringApp (Doncheva et al., 2019) with 0.7 confidence. MCODE clustering of the network was performed by Cytoscape (v3.7.2) and its plugin clusterMaker (Cline et al., 2007). GO and KEGG enrichment analyses of the network were performed via g:Profiler (Raudvere et al., 2019).

PLA

The Duolink PLA Kit (Sigma-Aldrich, 92101) was used based on the manufacturer's instructions. Briefly, HeLa S3 PCDH7-GFP-BAC cells were seeded onto glass coverslips and synchronized to cytokinesis with bipolar synchronization. The cells were fixed using 3.2% paraformaldehyde and permeabilized with 0.1% Triton X-100 in TBS. After blocking with Duolink blocking solution for 30 min at 37°C, the cells were incubated overnight at 4°C with corresponding pairs of primary antibodies: anti-GFP (Invitrogen, A11120, 1:1000) for PCDH7 and anti-ZDHHC5 (Sigma-Aldrich, HPA014670, 1:2000). Samples treated with only one corresponding primary antibody were used as controls. The cells were washed and incubated with PLA probes for 1 h at 37°C. After another wash, the cells were treated with the ligase for 30 min at 37°C. The washing step was repeated and the cells were incubated with the polymerase for 100 min at 37°C. After the final washes, the slides were mounted with a coverslip using the Duolink Mounting Medium with DAPI and incubated for 15 min before sealing.

GFP-trap pull-down assay for the protein interactions

HeLa S3 cells expressing GFP alone or PCDH7::GFP were arrested in mitosis and used for pull-down assays. The pellets were dissolved in PBS with 1% Triton X-100, EDTA-free protease inhibitor (Thermo Fisher Scientific/Pierce, 88666) and PhosSTOP (Roche, 4906845001), and then homogenized and centrifuged at 17,000 *g* for 10 min at 4°C. Protein concentrations were determined by BCA protein assay (Pierce, 23225) and equal protein amounts from each sample were loaded into pre-conditioned GFP-Trap A beads (gta-20; ChromoTek). Aliquots of the input sample were saved for further analysis. After incubation for 3 h at 4°C, the unbound samples were collected, the GFP-Trap A beads were washed and proteins were eluted in 2× Laemmli buffer with 100 mM DTT by boiling for 10 min at 95°C.

Western blotting analysis

Samples were separated by molecular mass using 10% SDS-PAGE gels and transferred to a nitrocellulose membrane. The membrane was blocked with 4% w/v nonfat dry milk in TBS containing 0.1% Tween-20 and probed with the primary antibody diluted in 2% BSA in TBS containing 0.1% Tween-20. The signal was visualized using ECL (Pierce, 32106; Bio-Rad, 1705061) detection of the HRP-conjugated secondary antibodies (Cell Signaling Technology, 7074S and 70765; 1:2000). The following primary antibodies were used for western blotting: anti-PCDH7 (Abcam, ab139274, 1:400), anti-EGFR (Santa Cruz Biotechnology, SC-03, 1:100), anti-tubulin (Cell Signaling Technology, 3873, 1:2000), anti-actin (Abcam, ab6276, 1:5000), anti-phospho-histone H3 (Upstate, 06-570, 1:500) and anti-biotin (custom antibody, 1:10,000), GFP (custom antibody, 1:5000), anti-ZDHHC5 (Atlas Antibodies, HPA014670, 1:2000) and anti-calnexin (Abcam, ab22595, 1:1000). Source data for all western blots are available in Fig. S7.

Detection of palmitoylation by ABE assay

For detection of protein palmitoylation, the ABE procedure was performed as previously described (Wan et al., 2007). Briefly, cell pellets were lysed in ice-cold lysis buffer [150 mM NaCl, 50 mM Tris-HCl, 5 mM EDTA, pH 7.4 with 10 mM NEM (Pierce, 23030), 1× protease inhibitor cocktail (PI) and 2× phenylmethylsulfonyl fluoride (PMSF; Cayman, 14333)]. After homogenization, membrane proteins were enriched by using high-speed centrifugation (Optima MAX-XP Ultracentrifuge, TLA-120.2 rotor) at 200,000 *g* for 30 min at 4°C. The membrane-enriched pellet was dissolved in lysis buffer with 10 mM NEM, 1× PI, 1× PMSF and 1.7% Triton X-100 and incubated at 4°C for 2 h. To remove particulates, the sample was centrifuged at 250 *g* for 5 min at 4°C. Chloroform-methanol (CM) precipitation was applied to precipitate the proteins. The pellet was air-dried for 2–3 min and 4% SDS buffer (4SB) (4% SDS, 50 mM Tris, 5 mM EDTA, pH 7.4) with 10 mM NEM was added into the sample and incubated for 20 min at 37°C to dissolve the protein pellet completely. After NEM incubation overnight at 4°C (1 mM NEM, 1× PI, 1 mM PMSF and 0.2% Triton X-100), three sequential CM precipitations were applied to remove NEM from the sample. After the final CM precipitation, the pellet was dissolved in 4SB, and the sample was equally divided into two fractions as HA− and HA+, and incubated for 1 h at room temperature with HA− [50 mM Tris, 1 mM HPDP–biotin (Thermo Fisher Scientific, 21341), 0.2% Triton X-100, 1 mM PMSF, 1× PI, pH 7.4] and HA+ (0.7 M hydroxylamine, 1 mM HPDP–biotin, 0.2% Triton X-100, 1 mM PMSF, 1× PI, pH 7.4) buffers, respectively. Then, proteins were precipitated by CM precipitation and the dissolved pellets were incubated in low HPDP–biotin buffer (150 mM NaCl, 50 mM Tris, 5 mM EDTA, 0.2 mM HPDP–biotin, 0.2% Triton X-100, 1 mM PMSF, 1× PI, pH 7.4) for 1 h at room temperature. Three sequential CM precipitations were performed to remove unreacted biotin. The protein pellets were dissolved in 4SB and then SDS was diluted to 0.1% by the addition of 0.2% Triton X-100, 1× PI and 1 mM PMSF, and samples were incubated at room temperature for 30 min. Then, samples were loaded on pre-conditioned Streptavidin Plus UltraLink Resin (Pierce, 53117) and incubated for 90 min at room temperature. Unbound fractions from both samples were saved, beads were washed three times with lysis buffer containing 0.1% SDS and 0.2% Triton X-100, and bound proteins were eluted in 2× Laemmli buffer with 1% β-mercaptoethanol by boiling for 10 min at 95°C.

Triton X-114 extraction

Hydrophobic proteins were extracted from the hydrophilic ones using the Triton X-114 (TX-114) extraction protocol as described previously

(Bordier, 1981; Taguchi et al., 2013). Briefly, precondensation of TX-114 (Biomatik, A4026) was performed by repeated cycles of clarifying at 4°C and incubation at 37°C to separate the detergent phase. Cells were lysed using lysis buffer (2% TX-114 in PBS), and the lysate was cleared by centrifugation at 16,100 *g* for 3 min at 4°C. The lysate was then centrifuged at 22,000 *g* for 10 min at room temperature for phase separation. The aqueous phase was removed, and the detergent phase was washed with wash buffer (0.1% TX-114 in PBS), clarified on ice, and incubated at 37°C for phase separation. Centrifugation and washing steps were repeated two more times and the detergent and aqueous phases were collected for further analysis.

Surface labeling and pull-down of cell surface proteins
Plasma membrane proteins were labeled with sulfo-NHS-SS-biotin for membrane enrichment as previously described (Özkan Küçük et al., 2018). Briefly, cells were incubated with 5 mM S-NHS-SS-biotin (Pierce, 21331) for 30 min at 4°C with gentle shaking, the reaction was quenched with glycine, and cells were snap frozen. Cells were lysed in a buffer (10 mM Tris-HCl pH 7.6, 0.5% SDS, 2% NP40, 150 mM NaCl, 1 mM EDTA and 10 mM iodoacetamide) supplemented with protease inhibitors (Pierce, 88666) and the lysates were incubated with pre-conditioned Streptavidin Plus UltraLink Resin overnight at 4°C. Unbound samples were collected and the beads were washed with lysis buffer three times. Biotinylated surface proteins were eluted by boiling at 70°C for 20 min in SDS sample buffer including 100 mM DTT with agitation. All fractions including whole-cell lysates (input) and unbound and plasma membrane-enriched (elute) fractions were analyzed by western blotting.

RNAi-mediated gene silencing
ZDHHC5 expression was knocked down using shRNA and siRNA approaches. shZDHHC5 was gifted by Dr G. Ekin Atilla-Gökcümen (Department of Chemistry, University at Buffalo, The State University of New York, Buffalo, USA) (Pradhan et al., 2021) and pLKO.1 was gifted by Dr Elif Nur Fırat Karalar (Department of Molecular Biology and Genetics, Koc University, Istanbul, Türkiye). The lentiviral particles of shZDHHC5 (target sequence 5′-CCCAGTTACTAACTACGGAAA-3′ in pLKO.1 vector) and empty pLKO.1 (Addgene, #8453) were packaged in HEK293T cells and used to transduce PCDH7-GFP-BAC cells. Virus-incorporated stable cells that stably expressed shRNAs were obtained after puromycin selection (2 μg/ml).

siGENOME siRNA pools that target *ZDHHC5* (siZDHHC5, Dharmacon, D-026577-01-0020, target sequence: 5′-GGACUAAGCCUGUAUGUGU-3') and non-targeting siRNA (Dharmacon, D-001210-01-05) were used for ZDHHC5 knockdown. PCDH7 expression was knocked down using different siRNA and esiRNA pools: FlexiTube GeneSolution for PCDH7 (QIAGEN, GS5099), FlexiTube siRNA PCDH7 6 (QIAGEN, SI03080469), FlexiTube siRNA PCDH7 5 (QIAGEN, SI03040261) and esiPCDH7 (Sigma-Aldrich, EHU077631). AllStars Negative Control siRNA (QIAGEN, 1027280) was used as control. All siRNAs were transfected with Lipofectamine RNAiMAX transfection reagent (Thermo Fisher Scientific) according to the manufacturer's instructions. Briefly, cells were seeded and transfected with 15 pmol of siRNA two times, at 24 h and 48 h. After 72 h after seeding, cells were either pelleted for western blotting analysis or fixed for immunofluorescence analysis.

CRISPR-based knockout
sgRNAs that target *PCDH7* were designed using the online 'CRISPR design tool' (http://crispr.mit.edu). The following oligonucleotide sequences were used as top/bottom pairs: sg1, 5′-CACCGCGACGTCCGCATCGG-CAACG-3′ and 5′-AAACCGTTGCCGATGCGGACGTCG-3′; sg5, 5′-CACCGCATCGTGACCGGATCGGGTG-3′ and 5′-AAACCACCCGAT-CCGGTCACGATG-3′; and sg6, 5′-CACCGCGGGCTTCTCTTTGGC-GCGC-3′ and 5′-AAACGCGCGCCAAAGAGAAGCCCGC-3′. All sgRNAs were cloned into the lentiCRISPR plasmid (Shalem et al., 2014) (pXPR_001; Addgene, #49535) as described in Ran et al. (2013).

PCDH7 knockout cell lines were generated by lipofectamine transfection of the CRISPR plasmid to HeLa S3 cells followed by

antibiotic selection. Single colonies were isolated with serial dilution of the pool population and PCDH7 knockout clones were selected after verifying the absence of PCDH7 protein expression with western blotting. CRISPR rescue cell lines were generated by viral transduction of the pLenti (Campeau et al., 2009) PCDH7::eGFP plasmid to PCDH7 knockout cells.

Author contributions
Conceptualization: N.E.O.K., N.O.; Methodology: N.E.O.K., B.N.Y., B.S.D., N.B.; Formal analysis: A. Kamacioglu, N.B., A. Kiraz; Investigation: N.E.O.K., N.O.; Resources: N.E.O.K., M.H.Q.; Data curation: N.E.O.K., B.N.Y., B.S.D., G.N.Y., N.B.; Writing - original draft: N.E.O.K., N.O.; Visualization: N.E.O.K.; Supervision: A. Kiraz, N.O.; Project administration: N.O.; Funding acquisition: N.O.

Data availability
The mass spectrometry proteomics data have been deposited to the ProteomeXchange Consortium via the PRIDE (Perez-Riverol et al., 2019) partner repository with the dataset identifier PXD029246.

First Person
This article has an associated First Person interview with the first author of the paper.

Peer review history
The peer review history is available online at https://journals.biologists.com/jcs/lookup/doi/10.1242/jcs.260266.reviewer-comments.pdf

References
Amano, M., Ito, M., Kimura, K., Fukata, Y., Chihara, K., Nakano, T., Matsuura, Y. and Kaibuchi, K. (1996). Phosphorylation and activation of myosin by Rho-associated kinase (Rho-kinase). *J. Biol. Chem.* **271**, 20246-20249. doi:10.1074/jbc.271.34.20246

Blaskovic, S., Blanc, M. and van der Goot, F. G. (2013). What does S-palmitoylation do to membrane proteins? *FEBS J.* **280**, 2766-2774. doi:10.1111/febs.12263

Bordier, C. (1981). Phase separation of integral membrane proteins in Triton X-114 solution. *J. Biol. Chem.* **256**, 1604-1607. doi:10.1016/S0021-9258(19)69848-0

Bovellan, M., Romeo, Y., Biro, M., Boden, A., Chugh, P., Yonis, A., Vaghela, M., Fritzsche, M., Moulding, D., Thorogate, R. et al. (2014). Cellular control of cortical actin nucleation. *Curr. Biol.* **24**, 1628-1635. doi:10.1016/j.cub.2014.05.069

Bradley, R. S., Espeseth, A. and Kintner, C. (1998). NF-protocadherin, a novel member of the cadherin superfamily, is required for Xenopus ectodermal differentiation. *Curr. Biol.* **8**, 325-334. doi:10.1016/S0960-9822(98)70132-0

Brownlee, C. and Heald, R. (2019). Importin α partitioning to the plasma membrane regulates intracellular scaling. *Cell* **176**, 805-815.e8. doi:10.1016/j.cell.2018.12.001

Campeau, E., Ruhl, V. E., Rodier, F., Smith, C. L., Rahmberg, B. L., Fuss, J. O., Campisi, J., Yaswen, P., Cooper, P. K. and Kaufman, P. D. (2009). A versatile viral system for expression and depletion of proteins in mammalian cells. *PLoS ONE* **4**, e6529. doi:10.1371/journal.pone.0006529

Chen, X., Molino, C., Liu, L. and Gumbiner, B. M. (2007). Structural elements necessary for oligomerization, trafficking, and cell sorting function of

paraxial protocadherin. *J. Biol. Chem.* **282**, 32128-32137. doi:10.1074/jbc. M705337200

Choi, H., Kim, S., Fermin, D., Tsou, C.-C. and Nesvizhskii, A. I. (2015). QPROT: Statistical method for testing differential expression using protein-level intensity data in label-free quantitative proteomics. *J. Proteomics* **129**, 121-126. doi:10. 1016/j.jprot.2015.07.036

Cline, M. S., Smoot, M., Cerami, E., Kuchinsky, A., Landys, N., Workman, C., Christmas, R., Avila-Campilo, I., Creech, M., Gross, B. et al. (2007). Integration of biological networks and gene expression data using Cytoscape. *Nat. Protoc.* **2**, 2366-2382. doi:10.1038/nprot.2007.324

Cramer, L. P. and Mitchison, T. J. (1997). Investigation of the mechanism of retraction of the cell margin and rearward flow of nodules during mitotic cell rounding. *Mol. Biol. Cell* **8**, 109-119. doi:10.1091/mbc.8.1.109

Cramer, L. P., Mitchison, T. J. and Theriot, J. A. (1994). Actin-dependent motile forces and cell motility. *Curr. Opin. Cell Biol.* **6**, 82-86. doi:10.1016/0955-0674(94)90120-1

Doncheva, N. T., Morris, J. H., Gorodkin, J. and Jensen, L. J. (2019). Cytoscape StringApp: network analysis and visualization of proteomics data. *J. Proteome Res.* **18**, 623-632. doi:10.1021/acs.jproteome.8b00702

Eggert, U. S., Mitchison, T. J. and Field, C. M. (2006). Animal cytokinesis: from parts list to mechanisms. *Annu. Rev. Biochem.* **75**, 543-566. doi:10.1146/annurev.biochem.74.082803.133425

Hannoush, R. N. and Arenas-Ramirez, N. (2009). Imaging the lipidome: omega-alkynyl fatty acids for detection and cellular visualization of lipid-modified proteins. *ACS Chem. Biol.* **4**, 581-587. doi:10.1021/cb900085z

Hu, C.-K., Coughlin, M., Field, C. M. and Mitchison, T. J. (2008). Cell polarization during monopolar cytokinesis. *J. Cell Biol.* **181**, 195-202. doi:10.1083/jcb. 200711105

Kahr, I., Vandepoele, K. and VAN Roy, F. (2013). Delta-protocadherins in health and disease. *Prog. Mol. Biol. Transl. Sci.* **116**, 169-192. doi:10.1016/B978-0-12-394311-8.00008-X

Kappel, C. and Eils, R. (2004). Fluorescence recovery after photobleaching with the Leica TCS SP2. *Confocal Appl. Lett.* **18**, 1-12.

Karayel, Ö., Şanal, E., Giese, S. H., Üretmen Kagıalı, Z. C., Polat, A. N., Hu, C.-K., Renard, B. Y., Tuncbag, N. and Özlü, N. (2018). Comparative phosphoproteomic analysis reveals signaling networks regulating monopolar and bipolar cytokinesis. *Sci. Rep.* **8**, 2269. doi:10.1038/s41598-018-20231-5

Karlsson, M., Zhang, C., Méar, L., Zhong, W., Digre, A., Katona, B., Sjöstedt, E., Butler, L., Odeberg, J., Dusart, P. et al. (2021). A single-cell type transcriptomics map of human tissues. *Sci. Adv.* **7**, eabh2169. doi:10.1126/sciadv.abh2169

Kim, S. H., Yamamoto, A., Bouwmeester, T., Agius, E. and Robertis, E. M. (1998). The role of paraxial protocadherin in selective adhesion and cell movements of the mesoderm during Xenopus gastrulation. *Development* **125**, 4681-4690. doi:10.1242/dev.125.23.4681

Kim, H., Takegahara, N. and Choi, Y. (2021). Protocadherin-7 regulates osteoclast differentiation through intracellular SET-binding domain-mediated RhoA and Rac1 activation. *Int. J. Mol. Sci.* **22**, 13117. doi:10.3390/ijms222313117

Kimura, K., Ito, M., Amano, M., Chihara, K., Fukata, Y., Nakafuku, M., Yamamori, B., Feng, J., Nakano, T., Okawa, K. et al. (1996). Regulation of myosin phosphatase by Rho and Rho-associated kinase (Rho-kinase). *Science* **273**, 245-248. doi:10.1126/science.273.5272.245

Kuroda, H., Inui, M., Sugimoto, K., Hayata, T. and Asashima, M. (2002). Axial protocadherin is a mediator of prenotochord cell sorting in Xenopus. *Dev. Biol.* **244**, 267-277. doi:10.1006/dbio.2002.0589

Lancaster, O. M., LE Berre, M., Dimitracopoulos, A., Bonazzi, D., Zlotek-Zlotkiewicz, E., Picone, R., Duke, T., Piel, M. and Baum, B. (2013). Mitotic rounding alters cell geometry to ensure efficient bipolar spindle formation. *Dev. Cell* **25**, 270-283. doi:10.1016/j.devcel.2013.03.014

Linder, M. E. and Deschenes, R. J. (2007). Palmitoylation: policing protein stability and traffic. *Nat. Rev. Mol. Cell Biol.* **8**, 74-84. doi:10.1038/nrm2084

Matsumura, F., Ono, S., Yamakita, Y., Totsukawa, G. and Yamashiro, S. (1998). Specific localization of serine 19 phosphorylated myosin II during cell locomotion and mitosis of cultured cells. *J. Cell Biol.* **140**, 119-129. doi:10.1083/jcb.140.1.119

Morishita, H. and Yagi, T. (2007). Protocadherin family: diversity, structure, and function. *Curr. Opin. Cell Biol.* **19**, 584-592. doi:10.1016/j.ceb.2007.09.006

Narumiya, S., Tanji, M. and Ishizaki, T. (2009). Rho signaling, ROCK and mDia1, in transformation, metastasis and invasion. *Cancer Metastasis Rev.* **28**, 65-76. doi:10.1007/s10555-008-9170-7

Neumann, B., Walter, T., Hériché, J.-K., Bulkescher, J., Erfle, H., Conrad, C., Rogers, P., Poser, I., Held, M., Liebel, U. et al. (2010). Phenotypic profiling of the human genome by time-lapse microscopy reveals cell division genes. *Nature* **464**, 721-727. doi:10.1038/nature08869

Nollet, F., Kools, P. and VAN Roy, F. (2000). Phylogenetic analysis of the cadherin superfamily allows identification of six major subfamilies besides several solitary members. *J. Mol. Biol.* **299**, 551-572. doi:10.1006/jmbi.2000.3777

Normand, G. and King, R. W. (2010). Understanding cytokinesis failure. *Adv. Exp. Med. Biol.* **676**, 27-55. doi:10.1007/978-1-4419-6199-0_3

Ohno, Y., Kihara, A., Sano, T. and Igarashi, Y. (2006). Intracellular localization and tissue-specific distribution of human and yeast DHHC cysteine-rich domain-containing proteins. *Biochim. Biophys. Acta* **1761**, 474-483. doi:10.1016/j.bbalip. 2006.03.010

Özkan Küçük, N. E., Şanal, E., Tan, E., Mitchison, T. and Özlü, N. (2018). Labeling carboxyl groups of surface-exposed proteins provides an orthogonal approach for cell surface isolation. *J. Proteome Res.* **17**, 1784-1793. doi:10.1021/acs.jproteome.7b00825

Ozlü, N., Monigatti, F., Renard, B. Y., Field, C. M., Steen, H., Mitchison, T. J. and Steen, J. J. (2010). Binding partner switching on microtubules and aurora-B in the mitosis to cytokinesis transition. *Mol. Cell. Proteomics* **9**, 336-350. doi:10.1074/mcp.M900308-MCP200

Ozlu, N., Qureshi, M. H., Toyoda, Y., Renard, B. Y., Mollaoglu, G., Özkan, N. E., Bulbul, S., Poser, I., Timm, W., Hyman, A. A. et al. (2015). Quantitative comparison of a human cancer cell surface proteome between interphase and mitosis. *EMBO J.* **34**, 251-265. doi:10.15252/embj.201385162

Perez-Riverol, Y., Csordas, A., Bai, J., Bernal-Llinares, M., Hewapathirana, S., Kundu, D. J., Inuganti, A., Griss, J., Mayer, G., Eisenacher, M. et al. (2019). The PRIDE database and related tools and resources in 2019: improving support for quantification data. *Nucleic Acids Res.* **47**, D442-D450. doi:10.1093/nar/gky1106

Phair, R. D., Gorski, S. A. and Misteli, T. (2004). Measurement of dynamic protein binding to chromatin in vivo, using photobleaching microscopy. *Methods Enzymol.* **375**, 393-414. doi:10.1016/S0076-6879(03)75025-3

Piekny, A. J. and Glotzer, M. (2008). Anillin is a scaffold protein that links Rhoa, actin, and myosin during cytokinesis. *Curr. Biol.* **18**, 30-36. doi:10.1016/j.cub. 2007.11.068

Plain, F., Howie, J., Kennedy, J., Brown, E., Shattock, M. J., Fraser, N. J. and Fuller, W. (2020). Control of protein palmitoylation by regulating substrate recruitment to a zDHHC-protein acyltransferase. *Commun. Biol.* **3**, 411. doi:10.1038/s42003-020-01145-3

Poser, I., Sarov, M., Hutchins, J. R. A., Hériché, J.-K., Toyoda, Y., Pozniakovsky, A., Weigl, D., Nitzsche, A., Hegemann, B., Bird, A. W. et al. (2008). BAC TransgeneOmics: a high-throughput method for exploration of protein function in mammals. *Nat. Methods* **5**, 409-415. doi:10.1038/nmeth.1199

Pradhan, A. J., Lu, D., Parisi, L. R., Shen, S., Berhane, I. A., Galster, S. L., Bynum, K., Monje-Galvan, V., Gokcumen, O., Chemler, S. R. et al. (2021). Protein acylation by saturated very long chain fatty acids and endocytosis are involved in necroptosis. *Cell Chem. Biol.* **28**, 1298-1309.e7. doi:10.1016/j. chembiol.2021.03.012

Qureshi, M. H., Bayraktar, H., Cinko, M. T., Akkaya, C., Kamacioglu, A., Uretmen-Kagiali, Z. C., Bozluolcay, E. and Ozlu, N. (2022). PCDH7 promotes cell migration by regulating myosin activity. *bioRxiv*, 2021.09. 21.460794.

Ramanathan, S. P., Helenius, J., Stewart, M. P., Cattin, C. J., Hyman, A. A. and Muller, D. J. (2015). Cdk1-dependent mitotic enrichment of cortical myosin II promotes cell rounding against confinement. *Nat. Cell Biol.* **17**, 148-159. doi:10. 1038/ncb3098

Ramkumar, N. and Baum, B. (2016). Coupling changes in cell shape to chromosome segregation. *Nat. Rev. Mol. Cell Biol.* **17**, 511-521. doi:10.1038/nrm.2016.75

Ran, F. A., Hsu, P. D., Wright, J., Agarwala, V., Scott, D. A. and Zhang, F. (2013). Genome engineering using the CRISPR-Cas9 system. *Nat. Protoc.* **8**, 2281-2308. doi:10.1038/nprot.2013

Rappsilber, J., Mann, M. and Ishihama, Y. (2007). Protocol for micro-purification, enrichment, pre-fractionation and storage of peptides for proteomics using StageTips. *Nat. Protoc.* **2**, 1896-1906. doi:10.1038/nprot.2007.261

Raudvere, U., Kolberg, L., Kuzmin, I., Arak, T., Adler, P., Peterson, H. and Vilo, J. (2019). g:Profiler: a web server for functional enrichment analysis and conversions of gene lists (2019 update). *Nucleic Acids Res.* **47**, W191-W198. doi:10.1093/nar/gkz369

Resh, M. D. (2006). Palmitoylation of ligands, receptors, and intracellular signaling molecules. *Sci. STKE* **2006**, re14. doi:10.1126/stke.3592006re14

Rieder, C. L. and Khodjakov, A. (2003). Mitosis through the microscope: advances in seeing inside live dividing cells. *Science* **300**, 91-96. doi:10.1126/science. 1082177

Rosenblatt, J. (2008). Mitosis: moesin and the importance of being round. *Curr. Biol.* **18**, R292-R293. doi:10.1016/j.cub.2008.02.013

Roux, K. J., Kim, D. I., Raida, M. and Burke, B. (2012). A promiscuous biotin ligase fusion protein identifies proximal and interacting proteins in mammalian cells. *J. Cell Biol.* **196**, 801-810. doi:10.1083/jcb.201112098

Shalem, O., Sanjana, N. E., Hartenian, E., Shi, X., Scott, D. A., Mikkelson, T., Heckl, D., Ebert, B. L., Root, D. E., Doench, J. G. and Zhang, F. (2014). Genome-scale CRISPR-Cas9 knockout screening in human cells. *Science* **343**, 84-87. doi:10.1126/science.124700

Söderberg, O., Gullberg, M., Jarvius, M., Ridderstråle, K., Leuchowius, K.-J., Jarvius, J., Wester, K., Hydbring, P., Bahram, F., Larsson, L.-G. et al. (2006). Direct observation of individual endogenous protein complexes in situ by proximity ligation. *Nat. Methods* **3**, 995-1000. doi:10.1038/nmeth947

Stewart, M. P., Helenius, J., Toyoda, Y., Ramanathan, S. P., Muller, D. J. and Hyman, A. A. (2011a). Hydrostatic pressure and the actomyosin cortex drive mitotic cell rounding. *Nature* **469**, 226-230. doi:10.1038/nature09642

Stewart, M. P., Toyoda, Y., Hyman, A. A. and Muller, D. J. (2011b). Force probing cell shape changes to molecular resolution. *Trends Biochem. Sci.* **36**, 444-450. doi:10.1016/j.tibs.2011.05.001

Stypulkowski, E., Asangani, I. A. and Witze, E. S. (2018). The depalmitoylase APT1 directs the asymmetric partitioning of Notch and Wnt signaling during cell division. *Sci. Signal.* **11**, eaam8705. doi:10.1126/scisignal.aam8705

Szklarczyk, D., Gable, A. L., Lyon, D., Junge, A., Wyder, S., Huerta-Cepas, J., Simonovic, M., Doncheva, N. T., Morris, J. H., Bork, P. et al. (2019). STRING v11: protein-protein association networks with increased coverage, supporting functional discovery in genome-wide experimental datasets. *Nucleic Acids Res.* **47**, D607-D613. doi:10.1093/nar/gky1131

Taguchi, Y., Mistica, A. M. A., Kitamoto, T. and Schätzl, H. M. (2013). Critical significance of the region between Helix 1 and 2 for efficient dominant-negative inhibition by conversion-incompetent prion protein. *PLoS Pathog.* **9**, e1003466. doi:10.1371/journal.ppat.1003466

Tai, K., Kubota, M., Shiono, K., Tokutsu, H. and Suzuki, S. T. (2010). Adhesion properties and retinofugal expression of chicken protocadherin-19. *Brain Res.* **1344**, 13-24. doi:10.1016/j.brainres.2010.04.065

Taubenberger, A. V., Baum, B. and Matthews, H. K. (2020). The mechanics of mitotic cell rounding. *Front. Cell Dev. Biol.* **8**, 687. doi:10.3389/fcell.2020.00687

Thilly, W. G. (1976). Maintenance of perpetual synchrony in HeLa S3 culture: theoretical and empirical approaches. *Methods Cell Biol.* **14**, 273-285. doi:10.1016/S0091-679X(08)60489-6

Toyoda, Y., Cattin, C. J., Stewart, M. P., Poser, I., Theis, M., Kurzchalia, T. V., Buchholz, F., Hyman, A. A. and Müller, D. J. (2017). Genome-scale single-cell mechanical phenotyping reveals disease-related genes involved in mitotic rounding. *Nat. Commun.* **8**, 1266. doi:10.1038/s41467-017-01147-6

Tsukita, S. and Yonemura, S. (1997). ERM (ezrin/radixin/moesin) family: from cytoskeleton to signal transduction. *Curr. Opin. Cell Biol.* **9**, 70-75. doi:10.1016/S0955-0674(97)80154-8

Uretmen Kagiali, Z. C., Saner, N., Akdag, M., Sanal, E., Degirmenci, B. S., Mollaoglu, G. and Ozlu, N. (2020). CLIC4 and CLIC1 bridge plasma membrane and cortical actin network for a successful cytokinesis. *Life Sci. Alliance* **3**, e201900558. doi:10.26508/lsa.201900558

Wadsworth, P. (2021). The multifunctional spindle midzone in vertebrate cells at a glance. *J. Cell Sci.* **134**, jcs250001. doi:10.1242/jcs.250001

Wan, J., Roth, A. F., Bailey, A. O. and Davis, N. G. (2007). Palmitoylated proteins: purification and identification. *Nat. Protoc.* **2**, 1573-1584. doi:10.1038/nprot.2007.225

Wang, C., Chen, A., Ruan, B., Niu, Z., Su, Y., Qin, H., Zheng, Y., Zhang, B., Gao, L., Chen, Z. et al. (2020). PCDH7 inhibits the formation of homotypic cell-in-cell structure. *Front. Cell Dev. Biol.* **8**, 329. doi:10.3389/fcell.2020.00329

Webb, Y., Hermida-Matsumoto, L. and Resh, M. D. (2000). Inhibition of protein palmitoylation, raft localization, and T cell signaling by 2-bromopalmitate and polyunsaturated fatty acids. *J. Biol. Chem.* **275**, 261-270. doi:10.1074/jbc.275.1.261

Woodley, K. T. and Collins, M. O. (2019). S-acylated Golga7b stabilises DHHC5 at the plasma membrane to regulate cell adhesion. *EMBO Rep.* **20**, e47472. doi:10.15252/embr.201847472

Woodley, K. T. and Collins, M. O. (2021). Regulation and function of the palmitoyl-acyltransferase ZDHHC5. *FEBS J.* **288**, 6623-6634. doi:10.1111/febs.15709

Yonemura, S., Nagafuchi, A., Sato, N. and Tsukita, S. (1993). Concentration of an integral membrane protein, CD43 (leukosialin, sialophorin), in the cleavage furrow through the interaction of its cytoplasmic domain with actin-based cytoskeletons. *J. Cell Biol.* **120**, 437-449. doi:10.1083/jcb.120.2.437

Yoshigaki, T. (1997). Accumulation of WGA receptors in the cleavage furrow during cytokinesis of sea urchin eggs. *Exp. Cell Res.* **236**, 463-471. doi:10.1006/excr.1997.3740

Zhou, X., Updegraff, B. L., Guo, Y., Peyton, M., Girard, L., Larsen, J. E., Xie, X. J., Zhou, Y., Hwang, T. H., Xie, Y. et al. (2017). PROTOCADHERIN 7 acts through SET and PP2A to potentiate MAPK signaling by EGFR and KRAS during lung tumorigenesis. *Cancer Res.* **77**, 187-197. doi:10.1158/0008-5472.CAN-16-1267-T